Toward consistency between trends in bottom-up CO_2 emissions and top-down atmospheric measurements in the Los Angeles megacity

S. Newman[1], X. Xu[2], K. R. Gurney[3], Y.-K. Hsu[4], K.-F. Li[5], X. Jiang[6], R. Keeling[7], S. Feng[8,*], D. O'Keefe[3], R. Patarasuk[3], K. W. Wong[8], P. Rao[8], M. L. Fischer[9], and Y. L. Yung[1]

[1]{Division of Geological and Planetary Sciences, California Institute of Technology, Pasadena, CA 91125, USA}
[2]{Department of Earth System Science, University of California, Irvine, CA 92697, USA}
[3]{School of Life Sciences, Arizona State University, Tempe, AZ 85287, USA}
[4]{Monitoring and Laboratory Division, Air Resources Board, Sacramento, CA 95811, USA}
[5]{Department of Applied Mathematics, University of Washington, Seattle, WA 98195, USA}
[6]{Department of Earth and Atmospheric Sciences, University of Houston, Houston, TX 77004, USA}
[7]{Scripps Institution of Oceanography, University of California, San Diego, La Jolla, CA 92037, USA}
[8]{Earth Atmospheric Science, Jet Propulsion Laboratory, California Institute of Technology, Pasadena, CA 91109}
[9]{Environmental Energy Area, E. O. Lawrence Berkeley National Laboratory, Berkeley, CA 94720, USA}

[*]{now at Department of Meteorology, Pennsylvania State University, University Park, PA 16802, USA}

Abstract

Large urban emissions of greenhouse gases result in large atmospheric enhancements relative to background that are easily measured. Using CO_2 mole fractions and $\Delta^{14}C$ and $\delta^{13}C$ values of CO_2 in the Los Angeles megacity observed in inland Pasadena (2006-2013) and coastal Palos Verdes peninsula (autumn 2009-2013), we have determined time series for CO_2 contributions from fossil fuel combustion (C_{ff}) for both sites and broken those down into contributions from petroleum/gasoline and natural gas burning for Pasadena. We find a 10 % reduction in Pasadena C_{ff} during the Great Recession of 2008-2010, which is consistent with the bottom-up inventory determined by the California Air Resources Board. The isotopic variations and total atmospheric CO_2 from our observations are used to infer seasonality of natural gas and petroleum combustion. The trend of CO_2 contributions to the atmosphere from natural gas combustion is out of phase with the seasonal cycle of total natural gas combustion seasonal patterns in bottom-up inventories but is consistent with the seasonality of natural gas usage by the area's electricity generating power plants. For petroleum, the inferred seasonality of CO_2 contributions from burning petroleum is delayed by several months relative to usage indicated by statewide gasoline taxes. Using the high-resolution Hestia-LA data product to compare C_{ff} from parts of the basin sampled by winds at different times of year, we find that variations in observed fossil fuel CO_2 reflect seasonal variations in wind direction. The seasonality of the local CO_2 excess from fossil fuel combustion along the coast, on Palos Verdes peninsula, is higher in fall and winter than spring and summer, almost completely out of phase with that from Pasadena, also because of the annual variations of winds in the region. Variations in fossil fuel CO_2

signals are consistent with sampling the bottom-up Hestia-LA fossil CO_2 emissions product for sub-city source regions in the LA megacity domain when wind directions are considered.

1 Introduction

Carbon dioxide is the most important greenhouse gas (GHG) contributing to current global warming, contributing 64 % of the total radiative forcing, according to the IPCC AR5 report (IPCC, 2013) and comprising 82 % of GHG emissions (NRC, 2010). The global average mole fraction of CO_2 has increased approximately 40 % since pre-industrial times due to anthropogenic emissions (IPCC, 2013). Since the proportion of the world's emissions from megacities (urban regions with more than 10 million inhabitants) is out of proportion with their small surface area (EDGAR, 2009; IEA, 2008), quantifying C_{ff} is essential if we are to work aggressively toward their reduction (Duren and Miller, 2012). As a consequence of global warming mitigation, reducing C_{ff} could reduce air pollution mortality, which is correlated with increased CO_2 levels (Jacobson, 2008).

Identifying the sources of emissions is a major first step in understanding and mitigating anthropogenic contributions. In cities, especially in megacities, these CO_2 sources often dominate over the normally predominant natural source of the biosphere, at least during certain seasons (e.g., Pataki et al., 2003; Widory and Javoy, 2003; Newman et al., 2013; 2008; Lopez et al., 2013; Turnbull et al., 2011; 2015; Vardag et al., 2015). The most common method of inventorying CO_2 emissions from human activities is through bottom-up reporting by governmental agencies, following IPCC methods (IPCC, 2013). Uncertainties in these methods range from 3-5 % to greater than 50 % (Andres et al., 2012). A more recent, scientifically-based bottom-up approach has been pioneered through the Vulcan and Hestia projects (Gurney et al., 2009; Gurney et al., 2012). These efforts combine multiple streams of data such as air pollution reporting, demographics,

property tax data, and traffic monitoring, to arrive at what is proving to be a much more accurate and space/time detailed estimate of fossil fuel CO_2 emissions. The Vulcan Project accomplished fossil fuel CO_2 emission estimation for the whole US at spatial scales of 10 km every hour of the year 2002, with updated years expected by the end of 2015. Hestia is specifically focused on the urban domain and has accomplished estimation down to the individual building and street segment scale for four cities (Indianapolis, IN; Salt Lake City, UT; Los Angeles basin, CA; Phoenix, AZ) with work ongoing in Baltimore, MD (Gurney et al., 2012, Patarasuk et al., in prep.; Rao et al., 2015). Both of these detailed data products are available for selected cities in the United States, facilitating top-down emissions quantification through long-term ambient air monitoring (Duren and Miller, 2012; Gurney et al., 2015). Trends in C_{ff} must be monitored precisely in order to evaluate progress towards mandated emission reductions. As an example, the California Global Warming Solutions Act of 2006 (Assembly Bill 32) requires reduction of greenhouse gas emissions to 1990 levels by 2020, a reduction of about 15 %. Indeed, now is the time to document the current level of emissions, as governments begin to implement strategies to reduce emissions (e.g., California's Cap-and-Trade Program and Low Carbon Fuel Standards) and want to be able to assess their efficacy.

Within megacities, atmospheric CO_2 concentrations are often highly elevated relative to the regional background due to locally emitted carbon dioxide. This excess can be analyzed for its isotopic composition to help attribute the local emissions to specific processes. Radiocarbon (^{14}C) analyses give quantitative information as to the proportions of CO_2 resulting from combustion of ancient sources of carbon (fossil fuels)

105 relative to sources incorporating modern carbon, such as the biosphere (e.g., Levin et al.,
106 2003; Levin and Roedenbeck, 2008; Turnbull et al., 2009), because of its short half-life
107 of 5730 years. The stable isotopes of carbon can be used to separate sources with
108 differing values, such as natural gas and petroleum combustion, with the $^{13}C/^{12}C$ ratio of
109 natural gas typically being lower than that of petroleum (e.g., Keeling, 1961; 1958;
110 Newman et al., 2008; 2013; Pataki et al., 2003; Widory and Javoy, 2003; Djuricin et al.,
111 2010; Moore and Jacobson, 2015), although there can be overlap between petroleum
112 combustion and biological respiration. Therefore, if we know the biosphere's
113 contribution from the fossil fuel CO_2 contribution derived from $\Delta^{14}C$ and the total CO_2
114 enhancement over background, we can distinguish all three sources (biosphere, petroleum
115 combustion, and natural gas combustion) provided that there are large variations, such as
116 in urban regions.

117 Here we report the use of ^{14}C combined with $\delta^{13}C$ in flask samples to disaggregate
118 the local emissions of CO_2 in the Los Angeles (LA) basin into biosphere, natural gas, and
119 petroleum combustion sources. We investigate the annual patterns and trends for 2006-
120 2013 in these components and compare them to global background and to bottom-up
121 inventories generated by government agencies and scientific colleagues. In particular, we
122 test the method against the changes in C_{ff} observed during and after the Great Recession
123 of 2008-2010 in LA.

124 The sampling, analytical methods, and calculations are described in section 2.
125 Section 3 discusses the results with regard to spatial and temporal variations and
126 comparison with bottom-up inventories and the detailed data product Hestia-LA. Overall
127 conclusions are presented in section 4.

2 Data and analysis

2.1 Locations

Samples were collected at two locations in the Los Angeles basin: on the campus of the California Institute of Technology (Caltech) in Pasadena, CA (34°8'12"N, 118°7'39"W, (240 ± 5) m above sea level), and on Palos Verdes peninsula overlooking the Pacific Ocean and Santa Catalina Island to the south (33°44.7'N, 118°20.9'W, 330 m above sea level) (Fig.1). Pasadena is located in the San Gabriel valley, approximately 14 km NE of downtown Los Angeles and 40 km from the coast. Prevailing winds from the SW bring marine air from the ocean during daytime hours, as the planetary boundary layer deepens during heating of the land. During these periods of prevailing south to west winds, the Palos Verdes site is a credible background site. Since the marine air picks up emissions from the basin during its transit inland, Pasadena is a good receptor site for LA emissions. The San Gabriel Mountains just 5 km to the north act as a barrier until midday, when upslope flow and the rising temperature inversion layer allow venting over the mountains (Lu and Turco, 1994; 1995).

2.2 Samples

Air samples were collected into evacuated one-liter Pyrex flasks through Synflex 1300 tubing after passing through $Mg(ClO_4)_2$ to dry the samples. In Pasadena, samples were collected on alternate afternoons at 1400 Pacific Standard Time (PST) using an autosampler, whereas at the Palos Verdes site samples were collected manually once a week (on weekend days) between 1100 and 1600 PST, and typically near 1400 PST. The

151 mid-afternoon sampling time was chosen because this is when the planetary boundary
152 layer tends to be the deepest and most well mixed during the day. The sampling path at
153 each location was purged with ambient air before collection.
154 CO_2 was extracted from the air samples cryogenically, following the methods described
155 in Newman et al. (2008), with the amount of CO_2 determined manometrically. Then the
156 $\delta^{13}C$ was determined relative to the Vienna PDB (VPDB) standard (Coplen, 1996) by
157 dual-inlet isotope ratio mass spectrometry (Thermo-Finnigan MAT 252; Bremen,
158 Germany) on each individual sample. After this analysis, the CO_2 was frozen into a cold
159 finger and combined with 3-7 other individual samples to create a composite sample
160 characterizing mid-afternoon air over a two-week (Pasadena) or month (Palos Verdes)
161 time period for $\Delta^{14}C$ analysis. This differs from the sampling protocol of Affek et al.
162 (2006), who collected on average two 5-liter samples per month, analyzed each sample
163 separately, and then averaged the results to produce monthly average $\Delta^{14}C$ values for
164 2004-2005. We found that by combining smaller samples collected more frequently
165 (alternate days in Pasadena) our results were less scattered than in the previous report and
166 therefore give interpretable seasonal variations. $\Delta^{14}C$ was analyzed by accelerator mass
167 spectrometer at the Keck-CCAMS facility at the University of California, Irvine, using
168 the methods described in Newman et al. (2013) and Xu et al. (2007). Analyses of air
169 from standard tanks calibrated by NOAA (National Oceanic and Atmospheric
170 Administration) gave errors for CO_2 mole fractions averaging of ± 1.4 ppm (1 ppm = 1
171 μmol mol^{-1}) (n = 44) and $\delta^{13}C$ of ± 0.15 ‰ (n = 30), including extraction, manometry,
172 and mass spectrometry. Although the uncertainties in the CO_2 mole fractions is much
173 higher than by spectroscopic techniques, it contributes less than half of the total

174 uncertainty in C_{ff}, which is dominated by the $\Delta^{14}C$ average error of 2 ‰, based on long-
175 term reproducibility of secondary standards (Xu et al., 2007; Xu et al., 2010; Graven et
176 al, 2013; Miller et al., 2013).

177

178 **2.3 Calculations**

179 A major goal of this study is the attribution of the sources of the C_{ff} observed. A
180 schematic figure of the flow of data used to calculate the portion of the total CO_2 that is
181 due to biosphere respiration (bio) and fossil fuel (ff) combustion, including burning of
182 petroleum (pet) and natural gas (ng), is shown in Fig. 2. Mole fractions of CO_2 measured
183 at the two sites and a background site in La Jolla, CA, were used to calculate the CO_2
184 excess (xs) over background (bg). The contributions of fossil fuel combustion and the
185 biosphere to the excess were determined from radiocarbon measurements, and the fossil
186 fuel component was further broken down into petroleum and natural gas using $\delta^{13}C$ of the
187 CO_2. Details are described below.

188

189 **2.3.1 Total CO_2 emissions and background CO_2 mole fraction**

190 The CO_2 excess caused by local emissions at the two sites was calculated by
191 subtracting an estimate of the background CO_2 mole fraction derived from La Jolla
192 monthly values (Keeling et al., 2005; Figs. 3 and 4). Flask sampling at La Jolla is done
193 so as to minimize the influence of local CO_2 sources by sampling during periods that
194 simultaneously satisfy three criteria: low variability in CO_2 concentration for periods of
195 3 hours or more, wind speed of 2.6 m s^{-1} or more from a narrow southwesterly to
196 westerly sector, and high visibility. That these methods successfully minimize influences

197 of local fossil-fuel emissions is indicated by the consistency of the annual radiocarbon
198 concentrations at La Jolla compared to clean stations both to the north and south in the
199 Northern Hemisphere (Graven, 2012). In this paper, therefore, the La Jolla data
200 presented are screened background data. The La Jolla data were interpolated to
201 determine the appropriate value for the midpoint of the range of collection dates included
202 in each $\Delta^{14}C$ sample, using the algorithm from Thoning et al. (1989), with two harmonic
203 terms, three polynomial terms, and the smoothed residuals of the long term trend (cutoff
204 of 667 days).
205

206 ### 2.3.2 CO_2 from fossil fuels, based on $\Delta^{14}C$

207 Mass balance calculations were used to calculate the relative contributions of
208 background air, biosphere respiration and photosynthesis, and fossil fuel combustion
209 (including natural gas and oil) to the CO_2 collected at the two sites. The following
210 equations quantitatively separate the background air, biosphere, and fossil fuel
211 combustion contributions to the locally measured atmospheric CO_2 using $\Delta^{14}C$ (e.g.,
212 Levin et al., 2003; Miller et al., 2012; Pataki et al., 2003; Turnbull et al., 2006; Fig. 4):

213 $$C_{obs} = C_{bg} + C_{ff} + C_r + C_p \quad (1)$$

214 $$\Delta_{obs}C_{obs} = \Delta_{bg}C_{bg} + \Delta_{ff}C_{ff} + \Delta_r C_r + \Delta_p C_p \quad (2)$$

215 where subscripts obs, bg, ff, r and p indicate observed, background, fossil fuels,
216 respiration, and photosynthesis, respectively, C indicates CO_2 mole fraction in ppm, and
217 Δ indicates $\Delta^{14}C$ in ‰. We assume that Δ_p is equivalent to Δ_{bg}, since natural
218 fractionation during uptake is corrected in the $\Delta^{14}C$ measurement and therefore substitute

219 Δ_{bg} for Δ_p in Eq. (2). Then, after solving Eq. (1) for C_p and substituting this for C_p in Eq.
220 (2), we solve Eq. (2) for C_{ff}, resulting in the following expression for C_{ff}:

221 $$C_{ff} = \frac{C_{obs}(\Delta_{obs}-\Delta_{bg})}{\Delta_{ff}-\Delta_{bg}} - \frac{C_r(\Delta_r-\Delta_{bg})}{\Delta_{ff}-\Delta_{bg}} \qquad (3)$$

222 The value of Δ_{ff} is -1000 ‰, since fossil fuels contain no ^{14}C because they have been
223 removed from the source of this short-lived radionuclide for millions of years.

224 We use the record from Pt. Barrow, AK (Xiaomei Xu, unpublished data) for the
225 concurrent background $\Delta^{14}C$ values (Δ_{bg}), because this is the most complete record
226 available for the entire time period of this study. The background $\Delta^{14}C$ record at Pt.
227 Barrow, AK is obtained through the UCI/NOAA ESRL (Earth System Research
228 Laboratory) flask network program that collects whole air samples using 6-L, 1-valve
229 stainless steel canisters (Silco Can, Restek Co.) that have been pre-evacuated at UCI. The
230 canisters are pressurized to ~2 atm using an oil-free pump. Two biweekly samples were
231 collected before 2008, and one weekly afterwards. For the period from 17 June 2005 to
232 17 March 2006, some duplicate samples were collected using 32-L, 1-valve stainless steel
233 canisters. Subsamples were then taken from these samples for ^{14}C analysis. CO_2 is
234 extracted cryogenically at UCI then converted to graphite by the sealed tube zinc
235 reduction method (Xu et al. 2007). Each sample is ~2.7 mg C in size. Analysis of $\Delta^{14}C$ is
236 performed at the W M Keck AMS facility at UCI with total measurement uncertainty of
237 ±1.3–2.4‰. Mass dependent fractionation is corrected for using "on-line" $\delta^{13}C$
238 measurements during AMS analysis, which accounts for fractionation that occurred
239 during graphitization and inside the AMS. Comparison was made of 22 common sample
240 dates spanning 5 yr, of measured $\Delta^{14}C$ from Barrow between the UCI and the Scripps
241 Institution of Oceanography's CO_2 Program. It shows differences in measured $\Delta^{14}C$ are

242 consistent with the reported uncertainties and there is no significant bias between the
243 programs (Graven et al., 2013). Another inter-comparison is that of AMS-based
244 atmospheric $^{14}CO_2$ measurements organized by the NOAA Earth System Research
245 Laboratory, Boulder, Colorado. The UCI lab is one the three groups having inter-
246 laboratory comparability within 1‰ for ambient level $^{14}CO_2$ (Miller et al. 2013).
247 Comparison of the Pt. Barrow data with those from La Jolla (Graven et al., 2012; Fig. 5)
248 shows good agreement for 2004-2007, when the two data sets overlap. Comparing the
249 calculated values for C_{ff} from these two backgrounds and propagating through the time
250 series calculations (Section 3.4) results in a difference of approximately 1 % of the signal
251 we are measuring. We calculate C_{bio} (the sum of C_r and C_p) from Eq. (1), using the
252 calculated values of C_{ff} and the independent estimates of C_{bg} from the La Jolla data, so
253 that we understand the contribution of the biosphere to total local emissions.
254 The nuclear power plant contribution, the only other source of ^{14}C, is small on the
255 west coast of the U.S. (Graven and Gruber, 2011) and therefore is ignored.
256 Following Turnbull et al. (2006) and Miller et al. (2012), the respiration terms in
257 the equations above are assumed to reflect contributions due to heterotrophic respiration.
258 Thus, the second term in Eq. (3) is small in magnitude and is due to heterotrophic
259 respiration, through which microbes respire CO_2 that was from carbon previously
260 incorporated through photosynthesis. This term takes into account the isotopic
261 disequilibrium due to the significant time delay between photosynthetic incorporation and
262 respiration, assumed to be 10 years on average (Miller et al., 2012). The magnitude of
263 this correction for our urban Pasadena site is different relative to sites with smaller
264 anthropogenic CO_2 signals, since the CO_2 photosynthesized into the plant a decade ago

265 was not close to the background air composition of that time but was the local, "polluted"
266 air. The Δ_r in Eq. (3) for each sample was calculated by extrapolating the Pasadena trend
267 back 10 years. Because of the mild climate in southern California, we used a constant
268 value of C_r = 5 ppm, the same value used for summer by Turnbull et al. (2006). This
269 should be taken as an upper limit for this urban region. The range of the correction for
270 the second term in Eq. (3), including the sign, was -0.06 – -0.11 ppm, generally smaller
271 relative to regions where the biosphere contribution C_r is large (Miller et al., 2012;
272 Turnbull et al., 2006). For the data from the Palos Verdes site, we calculated the
273 heterotrophic correction term using values of Δ_r calculated by extrapolating the Pt.
274 Barrow background trend back 10 years and used a constant value of C_r = 5 ppm, because
275 of the mild climate. The correction term for the Palos Verdes data ranged from 0.20 –
276 0.24 ppm. The small correction for heterotrophic respiration does not affect any of our
277 conclusions.

278 In California, there is an added complication when attributing CO_2 emissions to
279 fossil fuels using $\Delta^{14}C$. Since 2004, 10 % ethanol has been added to gasoline. The
280 ethanol contains modern, not fossil, carbon. For gasoline with 10 % ethanol, 6.7 % of the
281 CO_2 emitted during combustion is from the modern ethanol (EIA, 2015). A correction
282 for this is made, as discussed in section 2.3.3 below.
283

284 **2.3.3 $\delta^{13}C$ of CO_2**

285 Plots involving the mole fractions and $\delta^{13}C$ can be used to determine $\delta^{13}C$ of the
286 local contribution to the observed CO_2 (Fig. 3). Here we use the Miller-Tans approach
287 (Miller-Tans approach; MT; Miller and Tans, 2003) for this purpose, since it allows for

variations in background composition and we observe a widening difference between the data for $\delta^{13}C$ in Pasadena and the La Jolla background record in recent years (Fig. 3e). The following mass balance equations are used in this analysis:

$$C_{obs} = C_{bg} + C_{src} \quad (4)$$

$$\delta_{obs} * C_{obs} = \delta_{bg} * C_{bg} + \delta_{src} * C_{src} \quad (5)$$

to give

$$\delta_{obs} * C_{obs} - \delta_{bg} * C_{bg} = \delta_{src}(C_{obs} - C_{bg}) \quad (6)$$

(Miller and Tans, 2003), where the subscript src represents the local source of CO_2 emissions, δ represents $\delta^{13}C$, and the appropriate background values are included for each sample. Using this formulation (Eq. 6), the slope of the correlation (MT slope) gives the $\delta^{13}C$ of this local source. For this analysis, we calculated the MT slopes for each month and then determined the seasonal averages, averaging December-January-February as winter, March-April-May as spring, June-July-August as summer, and September-October-November as autumn. Seven individual samples, over the eight-year sampling period in Pasadena, were excluded since they fell more than three times the standard error from their linear regression best-fit lines. The monthly MT plots for 2011 are shown in Fig. A1, as examples. The very high correlation coefficients (R = 0.952 – 0.999) suggest that δ_{src} remains constant on time scales of a month. We assume that this is also the case for the isotopic compositions of petroleum and natural gas combustion, that we describe below.

We use the results from the $^{14}CO_2$ calculations for the fraction of C_{xs} from the biosphere ($F_{bio} = 1 - F_{ff}$) together with the MT slopes to attribute the CO_2 derived from

petroleum and natural gas combustion (C_{pet} and C_{ng}) by mass balance, first by calculating the $\delta^{13}C$ of the fossil fuel component, using:

$$\delta_{ff} = \frac{\delta_{xs} - \delta_{bio}*(1-F_{ff})}{F_{ff}} \quad (7)$$

where F_{ff} is the fraction of C_{xs} due to emissions from fossil fuel combustion, as calculated from the $^{14}CO_2$ data. The values for δ_{xs} are the seasonal $\delta^{13}C$ values from the MT analyses and δ_{bio} is taken to be -26.6 ‰, the average $\delta^{13}C$ of the ambient air plus the discrimination of -16.8 ‰ for the biosphere (Bakwin et al., 1998). This value represents data from temperate northern latitudes (28 – 55 °N), dominated by C3 plants with some C4 grasses present (Bakwin, et al., 1998). Indeed, grasses in southern California are mostly C3 ryes, fescue, and bluegrass, with some C4 grasses such as St. Augustine (www.cropsreview.com/c3-plants.html, last accessed January 25, 2016). The proportions of CO_2 emitted by petroleum and natural gas combustion are calculated using the $\delta^{13}C$ values:

$$\delta_{ff} = F_{pet\,ff} * \delta_{pet} + (1 - F_{pet\,ff}) * \delta_{ng} \quad (8)$$

$$F_{pet\,ff} = \frac{\delta_{ff} - \delta_{ng}}{\delta_{pet} - \delta_{ng}} \quad (9)$$

with an analogous equation for $F_{ng\,ff}$. where $F_{pet\,ff}$ and $F_{ng\,ff}$ are the fractions of petroleum and natural gas combustion contributions in C_{ff}, respectively. The values of δ_{ng} and δ_{pet} used were -40.2±0.5 ‰ for natural gas (Newman et al., 2008; covering measurements in 1972-1973 and 1999) and -25.5±0.5 ‰ for petroleum combustion (average of measurements in (Newman et al., 2008; measurements in 2005), and -26.0, -25.1, and -25.5 ‰ measured in 2007, 2012, and 2014, respectively). The C_{ff}, C_{pet}, and C_{bio} components were corrected for the presence of 10 % ethanol in California gasoline by

multiplying C_{pet} by 0.067 (the fraction of CO_2 emitted by burning the ethanol portion of the ethanol-gasoline mixture; EIA, 2015) to give the amount, in ppm, of CO_2 that was included in C_{bio} but should have been attributed to C_{pet}. The same amount was deducted from C_{bio}. The magnitude of this correction is 0.5 – 1.2 ppm, averaging 0.84 ppm, which represents approximately a quarter of the C_{bio}, but the latter is very small, averaging 3 – 4 ppm and the correction does not affect our results with respect to C_{pet} and C_{ng}.

2.3.4 Time series analysis

We used the algorithm of Jiang et al. (2008) to study details of the average annual patterns of the total CO_2 and C_{ff} in Pasadena, in order to compare with patterns at sites with less contribution from regional fossil fuel combustion, such as Palos Verdes and La Jolla background. This method uses the first three Legendre polynomials and harmonic terms to decompose the signal (Prinn et al., 2000). The harmonic terms define the seasonal and semi-annual cycles, which we compared to results of the same analysis for flask data from La Jolla, CA (Keeling et al., 2005).

To determine trends in the C_{ff} time series, derived from the radiocarbon data, we used the empirical mode decomposition (EMD) method (Huang et al., 1998; Kobayashi-Kirschvink et al., 2012). Using this method, nonlinear and nonstationary time series can be broken down into intrinsic mode functions (IMFs) with increasing period lengths and, finally, to a long-term trend with at most only one minimum or maximum with slope of zero. The algorithm involves using cubic splines to calculate maximum and minimum envelopes for the data series. The average of these envelopes for each time is subtracted from the original or the previous iteration. This process is repeated until the average is a

355 horizontal line, giving the first IMF. This IMF is subtracted from the raw time series (or
356 previous starting point) and then repeated until the resulting IMF has only one maximum
357 or minimum in the series, the long-term trend. High frequency modes are removed first,
358 with the earliest representing noise. The later modes are interpreted in terms of known
359 processes, such as annual cycles (e.g., IMFs 3 and 4). Following Wu and Huang (2009),
360 we added random noise equivalent to the error in the measurements to create 300 time
361 series, for which the ensemble EMD (EEMD) analyses were averaged. The EEMD
362 technique is data adaptive, not assuming any shape for the IMFs.
363

364 ## 3 Results and discussion

365 The purpose of this project was to determine the sources of C_{ff} in the Los Angeles
366 basin and compare them with bottom-up inventories and data products from government
367 agencies and the scientific community. Below, we compare results of source allocation
368 from the two sites and then examine the temporal variability at the Pasadena site, with its
369 8-year record. Then we compare the results with government inventories and with the
370 high-resolution Hestia-LA emissions product.
371

372 ### 3.1 Spatial variations – comparison of source attribution at the Pasadena
373 and Palos Verdes sites

374 The $\Delta^{14}C$ time series for the two sites are shown in Fig. 3c and d, 8 years for
375 Pasadena and 4 years for Palos Verdes. The two data sets are very different, with Palos
376 Verdes radiocarbon results being significantly higher than those in Pasadena except
377 during the winter. However, the summer months in Pasadena are characterized by $\Delta^{14}C$
378 values far from background, i.e., depleted in ^{14}C due to dilution by CO_2 produced by

burning of fossil fuels containing none of the radioactive isotope. There are occasional negative spikes in $\Delta^{14}C$ during the winter. Total CO_2 excess (C_{xs}; Fig. 4), determined as CO_2 concentration minus background, is similarly disparate with respect to timing. The total enhancement at both Pasadena and Palos Verdes, C_{xs}, spikes during winter (up to 65 ppm and 34 ppm, respectively), but the Pasadena excess also peaks during the summer (up to 43 ppm), whereas Palos Verdes values for C_{xs} are at a minimum during the warm months (3-20 ppm). When the ^{14}C and C_{xs} information are combined to calculate CO_2 emissions due to fossil fuels (C_{ff}; eqn. 3; Fig. 4), we see summer maxima for C_{ff} in Pasadena, but not in Palos Verdes. The spikes in C_{xs} and C_{ff} during fall and winter seasons are not the general trend in Pasadena, as evidenced by the quarterly averages (Fig. 6b). The amount of C_{ff} in the Pasadena seasonal averages (Fig. 4a, 6b) ranges from (18.9 ± 1.2) ppm (winter) to (26.8 ± 0.4) ppm (summer). In Palos Verdes, C_{ff} averages (5 ± 3) ppm during the warmer months and (12 ± 5) ppm during the winter months (Fig. 4b). However, CO_2 emissions from the biosphere (C_{bio}) tend to be higher during the cooler months at both sites (Fig. 4). Refer to Section 3.2 for more discussion of the biosphere's contribution to C_{xs} in Pasadena.

The explanation for the differences in the seasonal cycles of C_{xs} and C_{ff} at the two sites is probably the different wind patterns for the different times of year. Figure 7 shows back trajectories ending at 1400 PST in Pasadena (Fig. A2 for both sites), calculated using NOAA's HYSPLIT model (Draxler and Rolph, 2014; Rolph, 2014), for January and July 2011. These are representative of these months in all years of this study. Wind directions during July are from the west-southwest, whereas they are mostly from the northeast but much more varied during the winter. Thus, in Pasadena, elevated

C_{xs} and C_{ff} values during the summer result from air masses traveling across the Los Angeles basin, picking up emissions and transporting them inland. During the winter, the airflow is more mixed, resulting in lower average C_{ff} signals in Pasadena, since a significant proportion of the winds bring less polluted air from the much less populated mountains and deserts located to the north (Santa Ana winds) (Fig. 7). The summer westerly winds bring ocean air to the Palos Verdes site, characterized by CO_2 mole fractions and $\Delta^{14}C$ very similar to background marine air. During the cooler months, the Santa Ana winds from the northeast occasionally blow over the LA basin, bringing its emissions to the coastal site (Fig. 7). This pattern results in more scatter in the magnitude of CO_2 excess observed during the winter at the Palos Verdes site, than during the summer. Figure 8 shows the average annual pattern for C_{ff} at the two sites, demonstrating the effect of the varying wind direction patterns.

3.2 Attribution of CO_2 excess from different anthropogenic sources for Pasadena

Since we have information regarding the relative contributions of fossil fuel combustion and biosphere respiration from the radiocarbon data, we can use the differences in the $\delta^{13}C$ of the CO_2 to look at the contributions of petroleum/gasoline versus natural gas combustion. We use the MT approach to distinguish between different fossil fuel sources of CO_2 (Miller and Tans, 2003). As described in section 2.3.3, the MT slope of the correlation gives the $\delta^{13}C$ of the local source of CO_2 emissions. In many cases it is difficult to distinguish the anthropogenic sources because the biosphere's signal can overlap that of petroleum. However, in a megacity such as the Los Angeles

425 basin, the contribution of the biosphere to the total CO_2 enhancement can be minimal
426 (≤20 % in Pasadena; Newman et al., 2008; Newman et al., 2013) during the afternoon,
427 when the boundary layer is deepest and most thoroughly mixed. In this study, we use the
428 information from $\Delta^{14}C$ presented above to further constrain the biosphere's input. Since
429 the other major anthropogenic sources (cement production and combustion of coal) are
430 not present in the Los Angeles basin, $\delta^{13}C$ from MT plots can be used to differentiate the
431 proportions of natural gas and oil burned in the region, as discussed below.
432 Seasonal MT slopes for the mid-afternoon Pasadena samples from 2006 through
433 2013 are shown in Fig. 6a. We do not present similar analysis for the Palos Verdes data
434 because it is a shorter data set, with only 3-5 measurements per month (12 per season),
435 and the range in CO_2 mole fractions during the warmer months is less than 20 ppm for all
436 spring and summer seasons. Thus there are insufficient meaningful data to produce a
437 significant trend. Vardag et al. (2015) came to this same conclusion for a rural site in
438 Germany, based on a modeling study.
439 The $\delta^{13}C$ values from MT regressions for the cooler portions of the year in
440 Pasadena are almost always higher than those for the warmer portions. The values for the
441 cooler seasons average (-30.6 ± 0.5) ‰, 1.8 ‰ higher than the average for the warmer
442 months, (-32.4 ± 0.6) ‰. Assuming that there is no contribution from respiration and
443 that the $\delta^{13}C$ of the high-CO_2 end members are -40.2 ‰ for natural gas and -25.5 ‰ for
444 petroleum combustion, as discussed above, then the proportion of natural gas burned in
445 C_{xs} is 32 % during the cooler months and 45 % during the warmer months. The larger
446 fraction of natural gas burned during the warm part of the year is consistent with the
447 observed burning of more natural gas for electricity generation during summer months, as

448 would be required to power air conditioning needs. Mild winters in this climate require
449 less natural gas combustion for heating buildings, thus minimizing a large winter peak
450 frequently seen in colder regions, such as Salt Lake City, UT (Pataki et al., 2003; Bush et
451 al., 2007) and Chicago, IL (Moore and Jacobson, 2015). This attribution of the different
452 contributions to C_{ff} still does require knowledge of the $\delta^{13}C$ value of the biosphere. As
453 mentioned above, we use a discrimination of 16.8 ‰, the average determined by Bakwin
454 et al. (1998) for northern mid-latitudes and includes a mix of C3 and C4 metabolism
455 plants, dominated by C3. More C4 plants will raise the C_{ng} curve and lower the C_{pet}
456 curve, since the discrimination by C4 plants is much lower (Farquhar et al., 1989).
457 As mentioned above, we can use the information provided by the $^{14}CO_2$ data to
458 put better constraints on contributions from the biosphere. The calculations based on
459 $\Delta^{14}C$ data in Fig. 6b show that the maximum biosphere contribution was during winter
460 2012-2013, 7 ppm (28 % of the total C_{ff}), and the minimum was 0.1 ppm during spring of
461 2010. The average is (4.1 ± 0.5) ppm (16 % of C_{ff}) during cooler months and (2.2 ± 0.3)
462 ppm (8 % of C_{ff}) during warmer months. The seasonality could be due to variations in
463 emissions from the biosphere. However, it is probably due to a more complex
464 combination of emissions and uptake.
465 The observation that there are seasonal patterns to the CO_2 emissions from
466 combustion of petroleum and natural gas has implications for the effective composition
467 of $\Delta^{14}C$ from fuel combustion. The value for fossil fuels is taken to be -1000 ‰, since
468 they contain no ^{14}C. However, because we have 10 % modern ethanol in our gasoline,
469 and there is seasonal variation in the ratio of gasoline to natural gas usage, there is
470 actually a seasonal variation in radiocarbon from the bulk fuel combustion component.

471 And at no time is the $\Delta^{14}C$ value actually that of pure fossil fuel (-1000 ‰). The average
472 value is -954 ‰, and spring-summer periods average 33 ‰ higher than autumn-winter
473 (-939 – -972 ‰, respectively). These seasonal and overall values for $\Delta^{14}C$ of the fuel
474 component were determined as the best-fit values from the individual C_{ff} data to the
475 seasonal mass balance calculations of C_{pet} and C_{ng}.
476
477 **3.3 Average seasonal and semi-annual patterns**
478 The emissions of CO_2 by anthropogenic processes significantly modifies the
479 annual cycle of CO_2 observed in the Los Angeles region relative to the oceanic air that
480 enters the basin, as exemplified by the background air sampled in La Jolla, CA (Keeling
481 et al., 2005; see discussion in section 2.3.1). There is very little seasonal variability in
482 Pasadena (Fig. 9a). Whereas the average background annual cycle is characterized by a
483 peak in April and drawdown in August-September, with an amplitude of 11 ppm (Fig.
484 9g), the Pasadena cycle is noisy and relatively flat, with lower CO_2 mole fractions in
485 January-April and high values the rest of the year and only an amplitude of 5 ppm (Fig.
486 9a). Each pattern can be modeled well using the Legendre polynomial/harmonic analysis
487 of Jiang et al. (2008; Fig. 9b, h). The sum of the seasonal and semi-annual harmonic
488 terms reproduces the data very well, with r^2 values of 0.70 and 0.91 for Pasadena and
489 background, respectively. The average annual cycles are 6 months out of phase, whereas
490 the semi-annual oscillation cycles look very similar at the two sites. The seasonal cycle
491 in Pasadena is consistent with influx of combustion CO_2 during the hot summer months
492 due to increased burning of natural gas at power plants located dominantly in the
493 southwestern portion of the LA basin (CEC, 2015). In contrast, the background data

494 reflect global patterns with a drawdown in CO_2 during the summer growing season in the
495 northern hemisphere. Jiang et al. (2012) concluded that the semi-annual oscillation at
496 NOAA's GLOBAL-VIEW sites is due to the combination of gross primary production
497 and respiration of the biosphere. During the winter season, photosynthesis is largely
498 reduced. The peak for gross primary production is relatively flat in winter. However,
499 CO_2 is still emitted to the atmosphere by respiration from the biosphere in winter, which
500 has a relatively sharp peak compared with the photosynthesis term. Thus the
501 combination of gross primary production and respiration leads to the double peaks in
502 each year in the net ecosystem production, which contributes to the semi-annual
503 oscillation in CO_2 (Jiang et al., 2012). The semi-annual oscillation in the background
504 signal is consistent with this interpretation. We see virtually the same pattern in
505 Pasadena, although the amplitude is smaller, consistent with the small biospheric
506 contribution indicated by the $\Delta^{14}C$ results.
507 Based on the work of Jiang et al. (2012) we expect the annual cycle in Pasadena
508 to be larger in amplitude than in La Jolla since it is further north, but the amplitude is
509 actually much smaller. If the regional emissions of CO_2 in Pasadena are relative to a La
510 Jolla background, then there is a huge enhancement during the summer! Indeed, the
511 seasonal cycle for C_{ff} (Fig. 8) is 11 ppm, with the peak in August-September, and there is
512 very little semi-annual oscillation.
513 The annual pattern for CO_2 in Palos Verdes is also heavily influenced by the
514 transport of combustion emissions from the Los Angeles basin (Fig. 7, 8, 9c, d). The
515 average monthly pattern is more similar to the background's (Fig. 9g, h) than to
516 Pasadena's (Fig. 9a, b). However, there is a strong peak in the winter that is consistent

517 with the increased number of days during this time of year with winds from the north to
518 east, travelling over the basin. Doing the same analysis for the monthly minimum values
519 (Fig. 9e, f) gives a pattern that is much more similar to the background's, confirmed by
520 the comparison of the raw data with the background smoothed time series in Fig. 3. This
521 supports use of minimum values from Palos Verdes as reasonable background for the Los
522 Angeles basin. The C_{ff} annual pattern is inverse to that in Pasadena, as expected by the
523 seasonal wind patterns (Figs. 7, 8).
524 The conclusion of this analysis of the annual cycles is that the Pasadena CO_2
525 pattern is significantly different from the natural cycles observed in La Jolla background
526 and show very little seasonal variation compared with this background. The semi-annual
527 pattern, although smaller in amplitude than expected, is in phase with that observed in the
528 background, which we suggest might reflect a reduced biosphere signature in Pasadena
529 due to artificial irrigation, which may reduce seasonality expected due to wet and dry
530 parts of the year. Both the Pasadena and Palos Verdes average CO_2 patterns reflect the
531 seasonal changes in wind patterns, whereas the monthly minimum Palos Verdes pattern is
532 that expected for the background air entering the LA basin. It will be interesting to see
533 whether water restrictions put into effect during summer of 2015 because of an on-going,
534 severe drought (ca.gov/drought, 2015), affect the patterns observed in the future.
535
536
537 **3.4 Temporal trends in CO_2 excess observed in Pasadena**
538 **3.4.1 Long-term time series analysis**
539 In order to discern the long-term trends in fossil-fuel CO_2 excess, we must first
540 remove noise and the periodic signals discussed above from the record. We used

empirical mode decomposition (EEMD; Huang et al., 1998; Kobayashi-Kirschvink et al., 2012), as described in the calculation section above, on the 8-year time series of C_{ff} (Fig. 4a) to identify intrinsic mode functions (IMFs; summary in Fig. 10a-d; full results in Fig. A3). The noise is represented by the first and second modes (IMF 1 and IMF 2). Combination of the third and fourth modes of the C_{ff} time series (IMF 3 and IMF 4) correlates significantly with the 30-day average record for temperature measured at the top of the 9-story library next to the sampling site ($r^2 = 0.6$). Note that there are severe mode mixing problems in IMF3 (e.g. during 2011–2013) between the dominant annual cycle and subseasonal variations, which also affects the nonlinear decompositions in the higher modes. To minimize the effects of mode mixing on the extractions of inter-annual trends, we perform the EEMD again after removing the average annual cycle (minus the mean of the raw data), defined as monthly averages over the entire time period (2006-2013; resulting time series shown in Fig. 10e). The revised inter-annual trend is shown in Fig. 10f. The sum of the trend + IMF 6 is a curve with increasing C_{ff} values leading up to mid-2007, when they began to fall, until leveling off in 2010 and perhaps starting to rise towards the end of the time series. There are end effects in this method, such that we do not have confidence in the first and last years of the analysis. The uncertainties in this calculation are shown by the shaded regions in Fig. 10f. These were determined as the 1σ standard deviations of adding random noise equivalent to 13.7 % to the data 300 times and then running the EMD analysis. The 13.7 % noise added is the uncertainty of the C_{ff} values calculated from $\Delta^{14}C$, ± 1 ppm, relative to the standard deviation of the data, 7.3 ppm. The maximum and minimum values are distinct at approximately the 2σ standard deviation level, as shown in Fig. 10f and indicate a significant decrease of 9.5 % between

564 the maximum in May 2007 and the average for January-June 2010. Using different
565 backgrounds for $\Delta^{14}C$, such as extrapolating the data from La Jolla (Fig. 5) does not
566 significantly affect this analysis, resulting in differences of (0.01 ± 0.09) ppm C_{ff} out of a
567 range on the order of 2 ppm. And our result showing that there are different values of
568 $\Delta^{14}C$ for bulk fuel for autumn-winter than for spring-summer also does not change these
569 conclusions, since the RMSE of the IMF6+trend (Fig. 10f) using different $\Delta^{14}C$ for cool
570 vs. summer months relative to the constant average value is 0.1 ppm C_{ff}.
571 The timing of the drop in the fossil-fuel CO_2 excess around 2008 is consistent
572 with the economic recession in late 2007-2009 (NBER, 2010) with slow recovery
573 beginning in 2010. Similar results for global CO_2 emissions due to fossil fuel combustion
574 have been documented by Peters et al. (2012) and Asefi-Najafabady et al. (2014). The
575 fraction of decrease in C_{ff} (9.5 %) is similar to, although less than, the decrease in global
576 GDP during this time (global GDP decreased by 13 %; World Bank, 2015).
577

578 **3.4.2 Comparison with inventories and bottom-up gridded C_{ff} data**

579 A major goal of this study is to compare trends in top-down measurements such
580 as those described here with bottom-up estimates in order to understand how to bring
581 them together in space and time for direct validation. Annual averages of the seasonal
582 amounts derived for C_{ff}, C_{pet}, and C_{ng} compare well in relative proportions to the averages
583 from California's state inventory provided by the California Air Resources Board
584 (CARB, 2015). Annual values for CO_2 emissions from all fossil fuels, on-road
585 transportation, and natural gas consumption for the entire state of California, through
586 2013, are superimposed on the seasonal averages for C_{ff}, C_{pet}, and C_{ng} in Fig. 11. The

587 decrease in total fossil fuels combustion between 2007 and 2011 in the State's inventory
588 is 11 %, very similar to the 9.5 % decrease indicated by the EEMD time series analysis of
589 our C_{ff} results above. There is a difference in timing between the data presented here
590 (2010) and those from the CARB inventory (2011-2012) that may be due to uncertainties
591 in the data or to the different domains covered by the two data sets. The relative
592 proportions of the on-road portion of the CARB budget is 57 % of fossil fuel CO_2
593 emissions and the petroleum portion of our top-down estimate averages 54 % of C_{ff}. This
594 inventory is for the entire state, not the LA basin, and it includes annual values only.
595 This discussion has focused on inter-annual variations in C_{ff}, although, as we have shown
596 in Fig. 7 and 8, there are at least seasonal variations in wind direction. Looking at back
597 trajectories from the entire time period of this study, we see no significant shifts in the
598 winds, from year to year although systematic modeling has not yet been done and is
599 beyond the scope of this paper. Next, we look at finer spatial and temporal scales.
600 Seasonal variations in C_{pet} concentration at the Pasadena location can be
601 compared to the variation in emissions compiled by various sources. Figure 12 presents a
602 comparison of the C_{pet} concentration to the petroleum and on-road CO_2 emissions
603 components estimated by the Energy Information Administration (EIA) (EIA, 2015), the
604 State of California (CARB, 2015), and the Hestia-LA project (K. R. Gurney, personal
605 communication). Comparison of the seasonal averages for petroleum consumption data,
606 based on deliveries (EIA), and gasoline taxes collected (CBE, 2014) with C_{pet} indicates
607 similar decreases of 10-20 %, but with a lag of a few months (Fig. 12). The lag could be
608 due to the different domains of the data sets: EIA and State of California data reflect the

609 entire state domain while the Hestia C_{ff} data product reflects the LA Basin specifically,
610 and the atmospheric data presented here represents air sampled in Pasadena.
611 To truly understand the observations in Pasadena, we must combine information
612 from spatial and temporal meteorological and C_{ff} databases, such as obtained using a
613 model like the Weather Research and Forecasting (WRF) model. Since this is beyond the
614 scope of this work, we have used the information from HYSPLIT back trajectories (Fig.
615 7; January and July) to provide rough limits for winds arriving in Pasadena at our
616 sampling time of 14:00 PST. These back trajectories suggest that prevailing winds
617 during the summer come from the southwest, across the basin, and winds during the
618 winter come from the northeast, across the mountains from the desert. We have looked at
619 1.3-km x 1.3-km gridded C_{ff} from the Hestia-LA data product to qualitatively determine
620 what relative emissions from petroleum combustion are expected during January and July
621 for the two years of the Hestia data (2011 and 2012). These are plotted in Fig. 12 and
622 agree in seasonality with the observations presented here: more C_{pet} is observed during
623 the summer than during the winter. A map of the regions selected for January (NE) and
624 July (SW) is presented in Fig. 13a, along with the HYSPLIT back trajectories for January
625 and July, 2011, and the monthly average CO_2 emissions due to total petroleum
626 combustion (the Hestia-LA product) from the two integrated areas based on the wind
627 directions are shown in Fig. 13b for years 2011 and 2012.
628 We show comparison of the C_{ng} results from Pasadena with area-integrated
629 bottom-up inventories and the Hestia-LA data product in Fig. 14. The California Energy
630 Commission (CEC, 2015) compiles data for natural gas consumed by power plants
631 throughout the state, including Los Angeles and Orange counties. These seasonal data

632 are consistent with the detailed Hestia-LA data for the electricity production for the entire
633 Los Angeles basin (dashed dark blue line in Fig. 14a). And the seasonality of all of the
634 inventories involving just the electrical power sector agrees well with the seasonality of
635 the time series for C_{ng} (Fig. 14a), with peaks during the summer and troughs during the
636 winter. The source attribution analysis using $\Delta^{14}C$ and $\delta^{13}C$ also captures the increase in
637 C_{ng} consumption of the power plants in recent years, although the data from this study
638 suggest that the increase started earlier than do the inventories. However, the
639 observations of CO_2 concentration and $\delta^{13}C$ integrate over all natural gas combustion and
640 cannot pick out just this one sector.

641 Overall statewide and Los Angeles basin inventories show maximum natural gas
642 usage during the winter (dashed green line in Fig. 14b). Other sources of combusted
643 natural gas include residential, commercial, industrial, and transportation use, which
644 could affect the trends, but we do not have seasonal data for these in the Los Angeles
645 megacity for the full period of this study. However, the seasonal signal for total
646 emissions from natural gas combustion from the Hestia-LA project for 2011-2012 is
647 consistent with the data presented here, when the seasonal prevailing wind directions are
648 considered. The seasonal pattern of emissions from natural gas combustion at any one
649 location is characterized by a small peak during the cooler months and a trough during
650 the warmer months (Fig. 13c). However, C_{ff} in the region sampled by winds arriving in
651 Pasadena during the winter (the northeast) are always lower than those in the basin, over
652 which the summer winds travel to the sampling site. Therefore, transport of air masses
653 following the seasonal wind patterns can explain the observations in Pasadena. The
654 earlier onset of the increase in C_{ff} from natural gas combustion indicated by the data

655 (2010) relative to that indicated by the government inventories might be due to the
656 mismatch in geographical regions, variations in inter-annual atmospheric transport, or
657 deficiencies in the inventories.

658 Since the seasonal cycle observed in C_{pet} and C_{ng} in Pasadena is probably due to
659 atmospheric transport, modeling of this effect is critical to being able to combine top-
660 down observations and bottom-up economic and usage data for a direct consistency
661 comparison. These effects must be removed in order to understand long-term trends due
662 to variations in anthropogenic emissions. The time series analysis using Empirical Mode
663 Decomposition presented in section 3.4.1 removes the seasonal signals to concentrate on
664 the longer-term signals, which show reasonable agreement with the longer-term trends in
665 the statewide inventory.

666

667 ## 4 Conclusion

668 Detection of anthropogenic excess of CO_2 at two sites in the Los Angeles basin,
669 one on the coast and one inland against a barrier mountain range, reveals significant
670 spatial and seasonal variability due to the biosphere, natural gas combustion, and
671 petroleum combustion. Seasonal patterns in wind direction determine the source region
672 of the excess detected at the two sites. Winds from the west to southwest during the
673 warmer months bring marine air with little excess to Palos Verdes, and these same winds
674 continue across the LA basin picking up emissions from fossil fuel combustion to be
675 observed in Pasadena. During the cooler months, wind directions are more varied and
676 include periods when air with low emissions comes to Pasadena from the northeast to

677 northwest and then travels across the basin to Palos Verdes, incorporating anthropogenic
678 emissions along the way.

679 The nature of the excess changes with season, as reflected by the $\delta^{13}C$ values of
680 CO_2 observed in Pasadena. During warmer months, lower values for $\delta^{13}C$ of the local
681 excess indicate a higher proportion of natural gas burned, consistent with government
682 inventories that indicate more natural gas burned during summer to produce electricity to
683 power air conditioning. Even more importantly, however, the seasonal trends in the
684 fossil fuel combustion observed in Pasadena are consistent with the shift from
685 southwesterly winds during warmer months to northeasterly winds during cooler months.
686 Therefore the source region of emissions changes from the Los Angeles basin during
687 summer to the mountains and desert during winter, for our Pasadena sampling site.
688 Trend analysis by ensemble empirical mode decomposition supports the relationship
689 between emissions and temperature.

690 The long-term trend in CO_2 excess from fossil fuel combustion is consistent with
691 C_{ff} changes associated with the economic recession and slow recovery of 2008 through
692 the present, and indicates a significant decrease of 9.5 % since the maximum in late 2007,
693 consistent with the bottom-up inventory of the California Air Resources Board. Indeed,
694 top-down and bottom-up methods of determining the anthropogenic sources of CO_2
695 emissions must be compared to each other to better understand inconsistencies, potential
696 biases, and uncertainty. Previously, however, comparisons have been limited by the
697 scope of emissions, large and overlapping uncertainty, and differences in the target
698 domain. Here we have shown that combining data from radiocarbon and $\delta^{13}C$ values
699 moves us towards a direct comparison in a megacity with very large emissions.

Measurement trends at a receptor site are consistent with annual variations in California statewide bottom-up inventories for C_{ff} attributed to petroleum and natural combustion, individually as well as for total CO_2 emissions. Even greater consistency between top-down measurements and granular emission estimates specific for the LA megacity domain are achieved when considering wind direction and sub-city source regions. This strengthens the need to have measurement, modeling, and inventories that are specifically aimed at the same domain with fine space/time resolution.

The next steps are to include modeling with inversion of the measurements to understand the combination of atmospheric transport and emissions and to extend the analysis to a denser network of surface monitoring stations such as the Los Angeles Megacities Carbon Monitoring Project (Kort et al., 2013) and the California Laboratory for Atmospheric Remote Sensing (CLARS) observations from Mount Wilson (Wong et al., 2015). Although the uncertainties are large enough that the method described here will not be usable in non-urban regions, similar to the conclusion of the modeling study by Vardag et al. (2015), anthropogenic C_{ff} dominate significantly over natural processes in megacities. Therefore, this kind of monitoring in megacities will allow society to understand and monitor the sources of the CO_2 that are the major contributors to global warming.

Acknowledgments

This work would not have been possible without support from the W.M. Keck Carbon Cycle Facility at UCI. We specifically thank J. Southon for his help with sample analysis. We acknowledge funding from the Keck Institute for Space Studies, NASA Grant NNX13AC04G, and NASA Grant NNX13AK34G. We also acknowledge funding

723 from the California Air Resources Board Contract #13-329. The statements and
724 conclusions in this report are those of the Contract and not necessarily those of the
725 California Air Resources Board. The mention of commercial products, their source, or
726 their use in connection with materials reported herein is not to be construed as actual or
727 implied endorsement of such products. The authors gratefully acknowledge the NOAA
728 Air Resources Laboratory (ARL) for providing the HYSPLIT transport and dispersion
729 model used in this publication. We thank N. C. Shu for hosting the site on the Palos
730 Verdes peninsula.

References

Andres, R. J., Boden, T. A., Bréon, F. M., Ciais, P., Davis, S., Erickson, D., Gregg, J. S., Jacobson, A., Marland, G., Miller, J., Oda, T., Olivier, J. G. J., Raupach, M. R., Rayner, P., and Treanton, K.: A synthesis of carbon dioxide emissions from fossil-fuel combustion, Biogeosciences, 9(5), 1845–1871, doi:10.5194/bg-9-1845-2012, 2012.

Affek, H. and Eiler, J.: Abundance of mass 47 CO_2 in urban air, car exhaust, and human breath, Geochim Cosmochim Acta, 70(1), 1–12, 2006.

Asefi-Najafabady, S., Rayner, P. J., Gurney, K. R., McRobert, A., Song, Y., Coltin, K., Huang, J., Elvidge, C., and Baugh, K.: A multiyear, global gridded fossil fuel CO_2 emission data product: Evaluation and analysis of results, J Geophy. Res-Atmos, 119, 10,213-10,231, doi:10.1002/2013JD021296, 2014.

Bakwin, P., Tans, P., White, J. and Andres, R.: Determination of the isotopic ($^{13}C/^{12}C$) discrimination by terrestrial biology from a global network of observations, Global Biogeochem Cycles, 12, 555-562, 1998.

Bush, S., Pataki, D., and Ehleringer, J.: Sources of variation in $\delta^{13}C$ of fossil fuel emissions in Salt Lake City, USA, Appl. Geochem, 2, 715-723, doi: 10.1016/j.apgeochem.2006.11.001, 2007.

CARB, California Air Resources Board: available at: http://www.arb.ca.gov/cc/inventory/data/data.htm (last access: July 2015), 2015.

CBE, California Board of Equalization: available at: http://www.boe.ca.gov/sptaxprog/reports/MVF_10_Year_Report.pdf (last access: November 2014), 2014.

CEC, California Energy Commission: available at: http://energyalmanac.ca.gov/electricity/web_qfer/Power_Plant_Statistical_Information.php (last access: January 2015), 2015.

Clark-Thorne, S. and Yapp, C.: Stable carbon isotope constraints on mixing and mass balance of CO_2 in an urban atmosphere: Dallas metropolitan area, Texas, USA, Applied Geochemistry, 18(1), 75–95, 2003.

Coplen, T. B.: Editorial: more uncertainty than necessary, Paleoceanography, 11, 369-370, 1996.

Djuricin, S., Pataki, D. E. and Xu, X.: A comparison of tracer methods for quantifying CO_2 sources in an urban region, J Geophys Res-Atmos, 115, D11303, doi:10.1029/2009JD012236, 2010.

Draxler, R.R. and Rolph: G.D.: HYSPLIT (HYbrid Single-Particle Lagrangian Integrated Trajectory) Model access via NOAA ARL READY Website (http://www.arl.noaa.gov/HYSPLIT.php). NOAA Air Resources Laboratory, College

767 Park, MD, 2014.
768
769 Duren, R. M. and Miller, C. E.: Measuring the carbon emissions of megacities, Nature
770 Climate Change, 2(8), 560–562, 2012.

771 EDGAR: European Commission, Joint Research Centre (JRC)/Netherlands
772 Environmental Assessment Agency (PBL). Emission Database for Global Atmospheric
773 Research (EDGAR), release version 4.0. http://edgar.jrc.ec.europa.eu (last access:
774 September 2015), 2009.

775 EIA (U.S. Energy Information Agency): Frequently asked questions: available at:
776 http://www.eia.gov/tools/faqs/faq.cfm?id=307&t=11, last access 4 September 2015.

777 Farquhar, G., Ehleringer, J. R., and Hubick, K. T.: Carbon isotope discrimination and
778 photosynthesis, Annu. Rev. Plant. Phys. Plant Mol. Biol., 40, 503–537, 1989.

779 Graven, H. D., and Gruber, N.: Continental-scale enrichment of atmospheric $^{14}CO_2$ from
780 the nuclear power industry: potential impact on the estimation of fossil fuel-derived CO_2,
781 Atmos Chem Phys, 11, 12339–12349, doi:10.5194/acp-11-12339-2011, 2011.

782 Graven, H. D., Guilderson, T. P. and Keeling, R. F.: Observations of radiocarbon in CO_2
783 at La Jolla, California, USA 1992–2007: Analysis of the long-term trend, J Geophys Res,
784 117, D02302, doi:10.1029/2011JD016533, 2012.

785 Graven, H., Xu, X., Guilderson, T. P., and Keeling R. F.: (2013), Comparison of
786 independent $\Delta^{14}CO_2$ records at Point Barrow, Alaska, Radiocarbon, 55, 1541–1545,
787 2013.

788 Gurney, K. R., I. Razlivanov, Y. Song, Y. Zhou, B. Benes, and M. Abdul-Massin:
789 Quantification of fossil fuel CO_2 emissions on the building/street scale for a large U.S.
790 city, Environ Sci Technol, 46, 12194-12202, dx.doi.org/10.1021/es3011282, 2012.

791 Gurney, K. R., Romero-Lankao, P., Seto, K. C., Hutyra, L. R., Duren, R., Kennedy, C.,
792 Grimm, N. B., Ehleringer, J. R., Marcutuillio, P., Hughes, S., Pincetl, S., Chester, M. V.,
793 Runfola, D. M., Feddema, J. J., and Sperling, J.: Climate change: Track urban emissions
794 on a human scale, Nature, *525*, 179–181, doi:10.1038/525179a, 2015.

795 Huang, N., Shen, Z. and Long, S.: The empirical mode decomposition and the Hilbert
796 spectrum for nonlinear and non-stationary time series analysis, Proc Royal Society
797 London Series A, 454, 903–995, 1998.

798 IEA: World Energy Outlook 2008, edited by: F. Birol, International Energy Agency.
799 2008.

800 IPCC: Climate Change 2013: The Physical Science Basis. Contribution of Working
801 Group I to the Fifth Assessment Report of the Intergovernmental Panel on Climate
802 Change [Stocker, T.F., D. Qin, G.-K. Plattner, M. Tignor, S.K. Allen, J. Boschung, A.

803 Nauels, Y. Xia, V. Bex and P.M. Midgley (eds.)]. Cambridge University Press,
804 Cambridge, United Kingdom and New York, NY, USA, 1535 pp., 2013.

805 Jacobson, M. Z.: On the causal link between carbon dioxide and air pollution mortality,
806 Geophys Res Lett, 35, L03809, doi:10.1029/2007GL031101, 2008.

807 Jiang, X., Li, Q., Liang, M.-C., Shia, R.-L., Chahine, M. T., Olsen, E. T., Chen, L. L. and
808 Yung, Y. L.: Simulation of upper tropospheric CO_2 from chemistry and transport models,
809 Global Biogeochem. Cy., 22, GB4025, doi:10.1029/2007GB003049, 2008.

810 Jiang, X., Chahine, M. T., Li, Q., Liang, M., Olsen, E. T., Chen, L. L., Wang, J. and
811 Yung, Y. L.: CO_2 semiannual oscillation in the middle troposphere and at the surface,
812 Global Biogeochem. Cy., 26, GB3006, doi:10.1029/2011GB004118, 2012.

813 Keeling, C.: The concentration and isotopic abundances of carbon dioxide in rural and
814 marine air, Geochim Cosmochim Acta, 24, 277–298, 1961.

815 Keeling, C. D.: The concentration and isotopic abundances of atmospheric carbon
816 dioxide in rural areas, Geochim Cosmochim Acta, 13(4), 322–334, doi:10.1016/0016-
817 7037(58)90033-4, 1958.

818 Kobayashi-Kirschvink, K. J., Li, K.-F., Shia, R.-L., and Yung, Y. L., Fundamental modes
819 of atmospheric CFC-11 from empirical mode decomposition, Adv Adapt Data Anal,
820 04(04), 1250024, doi:10.1142/S1793536912500240, 2012.

821 Kort, E. A., Angevine, W., Duren, R., Miller, C. E.: Surface observations for monitoring
822 urban fossil fuel CO_2 emissions: minimum site location requirements for the Los Angeles
823 megacity, J Geophys Res, 118, 1-8, doi: 10.1002/jgrd.50135, 2013.

824 Levin, I. and Roedenbeck, C.: Can the envisaged reductions of fossil fuel CO_2 emissions
825 be detected by atmospheric observations?, Naturwissenschaften, 95, 203–208,
826 doi:10.1007/s00114-007-0313-4, 2008.

827 Levin, I., Kromer, B., Schmidt, M. and Sartorius, H.: A novel approach for independent
828 budgeting of fossil fuel CO_2 over Europe by $^{14}CO_2$ observations, Geophys Res Lett,
829 30(23), 2194, 2003.

830 Lopez, M., Schmidt, M., Delmotte, M., Colomb, A., Gros, V., Janssen, C., Lehman, S. J.,
831 Mondelain, D., Perrussel, O., Ramonet, M., Xueref-Remy, I. and Bousquet, P.: CO, NO_x
832 and $^{13}CO_2$ as tracers for fossil fuel CO_2: results from a pilot study in Paris during winter
833 2010, Atmos Chem Phys, 13(15), 7343–7358, doi:10.5194/acp-13-7343-2013, 2013.

834 Lu, R. and Turco, R.: Air pollutant transport in a coastal environment. Part I: Two-
835 dimensional simulations of sea-breeze and mountain effects, Journal of the Atmospheric
836 Sciences, 51(15), 2285–2308, 1994.

837 Lu, R. and Turco, R.: Air pollutant transport in a coastal environment—II. Three-
838 dimensional simulations over Los Angeles basin, Atmos Environ, 29(13), 1499–1518,

1995.

Miller, J. and Tans, P.: Calculating isotopic fractionation from atmospheric measurements at various scales, Tellus B, 55, 207–214, 2003.

Miller, J. B., Lehman, S. J., Montzka, S. A., Sweeney, C., Miller, B. R., Karion, A., Wolak, C., Dlugokencky, E. J., Southon, J., Turnbull, J. C. and Tans, P. P.: Linking emissions of fossil fuel CO_2 and other anthropogenic trace gases using atmospheric $^{14}CO_2$, J Geophys Res, 117, D08302, doi:10.1029/2011JD017048, 2012.

Miller, J., Lehman, S., Wolak, C., Turnbull, J., Dunn, G., Graven, H., Keeling, R., H. Meijer, A., Aerts-Bijma, A. T., and Palstra, S. W.: Initial results of an intercomparison of AMS-based atmospheric $^{14}CO_2$ measurements, Radiocarbon, 55, 1475–1483, 2013.

Moore, J., and Jacobson, A. D.: Seasonally varying contributions to urban CO_2 in the Chicago, Illinois, USA region: Insights from a high-resolution CO_2 concentration and $\delta^{13}C$ record, Elem Sci Anth, 3, 000052, doi:10.12952/journal.elementa.000052.s004, 2015.

NBER, National Bureau of Economic Research: available at: http://www.nber.org/cycles/sept2010.html (last access: September 2010), 2010.

Newman, S., Xu, X., Affek, H. P., Stolper, E. and Epstein, S.: Changes in mixing ratio and isotopic composition of CO_2 in urban air from the Los Angeles basin, California, between 1972 and 2003, J Geophys Res-Atmos, 113, D23304, doi:10.1029/2008JD009999, 2008.

Newman, S., Jeong, S., Fischer, M. L., Xu, X., Haman, C. L., Lefer, B., Alvarez, S., Rappenglueck, B., Kort, E. A., Andrews, A. E., Peischl, J., Gurney, K. R., Miller, C. E. and Yung, Y. L.: Diurnal tracking of anthropogenic CO_2 emissions in the Los Angeles basin megacity during spring 2010, Atmos Chem Phys, 13(8), 4359–4372, doi:10.5194/acp-13-4359-2013, 2013.

NRC, National Research Council: Advancing the Science of Climate Change. National Research Council. The National Academies Press, Washington, DC, USA, 2010.

Pataki, D., Bowling, D. and Ehleringer, J.: Seasonal cycle of carbon dioxide and its isotopic composition in an urban atmosphere: Anthropogenic and biogenic effects, J Geophys Res, 108, 4735, 2003.

Patarasuk, R., Gurney, K. R., O'Keeffe, D., Song, Y., Huang, J., Rao, P., Buchert, M., Lin, J., Mendoza, D., and Ehleringer, J.: High-resolution fossil fuel CO_2 emissions quantification and application to urban climate policy, Urban Ecosys, in preparation, 2015.

Peters, G., Marland, G., Le Quéré, C. and Boden, T.: Rapid growth in CO_2 emissions after the 2008-2009 global financial crisis, Nature Climate Change, 2, 2-4, 2012.

875 Prinn, R. G., Weiss, R. F., Fraser, P. J., Simmonds, P. G., Cunnold, D. M., Alyea, F. N.,
876 O'Doherty, S., Salameh, P., Miller, B. R., Huang, J., Wang, R., Hartley, D. E., Harth, C.,
877 Steele, L. P., Sturrock, G., Midgley, P. M. and McCulloch, A.: A history of chemically
878 and radiatively important gases in air deduced from ALE/GAGE/AGAGE, J Geophys
879 Res-Atmos, 105(D14), 17751–17792, doi:10.1029/2000JD900141, 2000.

880 Rao, P., Gurney, K. R., Patarasuk, R., Song, Y., Miller, C. E., Duren, R. M. Duren, and
881 Eldering, A.: Spatio-temporal variations in onroad vehicle fossil fuel CO_2 emissions in
882 Los Angeles megacity, Environ. Sci. Technol., submitted, 2015.

883 Rolph, G.D. Real-time Environmental Applications and Display sYstem (READY)
884 Website: available at: http://www.ready.noaa.gov (last access: July 2015), NOAA Air
885 Resources Laboratory, College Park, MD, 2014.

886 Tans, P. P., Berry, J. A. and Keeling, R. F.: Oceanic 13C/ 12C observations: A new
887 window on ocean CO_2 uptake, Global Biogeochem Cycles, 7(2), 353–368,
888 doi:10.1029/93GB00053, 1993.

889 Thoning, K., Tans, P. and Komhyr, W.: Atmospheric carbon dioxide at Mauna Loa
890 Observatory, 2, Analysis of the NOAA/GMCC data, 1974-1985, J Geophys Res, 94(D6),
891 8549–8565, 1989.

892 Turnbull, J., Miller, J., Lehman, S., Tans, P., Sparks, R. and Southon, J.: Comparison of
893 $^{14}CO_2$, CO, and SF_6 as tracers for recently added fossil fuel CO_2 in the atmosphere and
894 implications for biological CO_2 exchange, Geophys Res Lett, 33, L01817,
895 doi:10.1029/2005GL024213, 2006.

896 Turnbull, J., Rayner, P., Miller, J., Naegler, T., Ciais, P. and Cozic, A.: On the use of
897 (CO_2)-C-14 as a tracer for fossil fuel CO_2: Quantifying uncertainties using an
898 atmospheric transport model, J Geophys Res-Atmos, 114, D22302,
899 doi:10.1029/2009JD012308, 2009.

900 Turnbull, J. C., Karion, A., Fischer, M. L., Faloona, I., Guilderson, T., Lehman, S. J.,
901 Miller, B. R., Miller, J. B., Montzka, S., Sherwood, T., Saripalli, S., Sweeney, C. and
902 Tans, P. P.: Assessment of fossil fuel carbon dioxide and other anthropogenic trace gas
903 emissions from airborne measurements over Sacramento, California in spring 2009,
904 Atmos Chem Phys, 11(2), 705–721, doi:10.5194/acp-11-705-2011, 2011.

905 Turnbull, J. C., Sweeney, C., Karion, A., Newberger, T., Lehman, S. J., Tans, P. P.,
906 Davis, K. J., Lauvaux, T., Miles, N. L., Richardson, S. J., Cambaliza, M. O., Shepson, P.
907 B., Gurney, K., Patarasuk, R. and Razlivanov, I.: Toward quantification and source sector
908 identification of fossil fuel CO_2 emissions from an urban area: Results from the INFLUX
909 experiment, J Geophys Res-Atmos, 120, 292–312, doi:10.1002/2014JD022555, 2015.

910 Vardag, S. N., C. Gerbig, G. Janssens-Maenhout, and I. Levin: Estimation of continuous
911 anthropogenic CO_2 using CO_2, CO, $\delta^{13}C(CO_2)$ and $\Delta^{14}C(CO_2)$, Atmos. Chem. Phys.
912 Discuss., 15(14), 20181–20243, doi:10.5194/acpd-15-20181-2015, 2015.

913 Widory, D. and Javoy, M.: The carbon isotope composition of atmospheric CO_2 in Paris,
914 Earth Planet Sci Lett, 215(1-2), 289–298, 2003.

915 Wong, K. W., Fu, D., Pongetti, T. J., Newman, S., Kort, E. A, Duren, R., Hsu, Y.-K.,
916 Miller, C. E., Yung, Y. L., and Sander, S. P.: Mapping CH_4:CO_2 ratio in Los Angeles
917 with CLARS-FTS from Mount Wilson, Atmos Chem Phys, 15, 241-252, 2015.

918 World Bank: GDP,
919 http://data.worldbank.org/indicator/NY.GDP.MKTP.CD/countries/1W-US?
920 display=graph, last access: May 2015.

921 Wu, Z. and Huang, N. E.: Ensemble empirical mode decomposition: A noise-assisted
922 data analysis method, Adv Adapt Data Anal, 1(01), 1–41, 2009.

923 Xu, X., Trumbore, S. E., Zheng, S., Southon, J. R., McDuffee, K. E., Luttgen, M. and
924 Liu, J. C.: Modifying a sealed tube zinc reduction method for preparation of AMS
925 graphite targets: Reducing background and attaining high precision, Nucl Instrum Meth
926 B, 259, 320–329, 2007.

927 Xu, X., Khosh, M. S., Druffel-Rodriguez, K. C., Trumbore S. E., and Southon J. R.:
928 (2010), Is the consensus value of ANU sucrose (IAEA C-6) too high? Radiocarbon, 52,
929 866-874, 2010.

930 York, R.: Asymmetric effects of economic growth and decline on CO_2 emissions, Nature
931 Climate Change, 2(11), 762–764, doi:10.1038/nclimate1699, 2012.

FIGURES

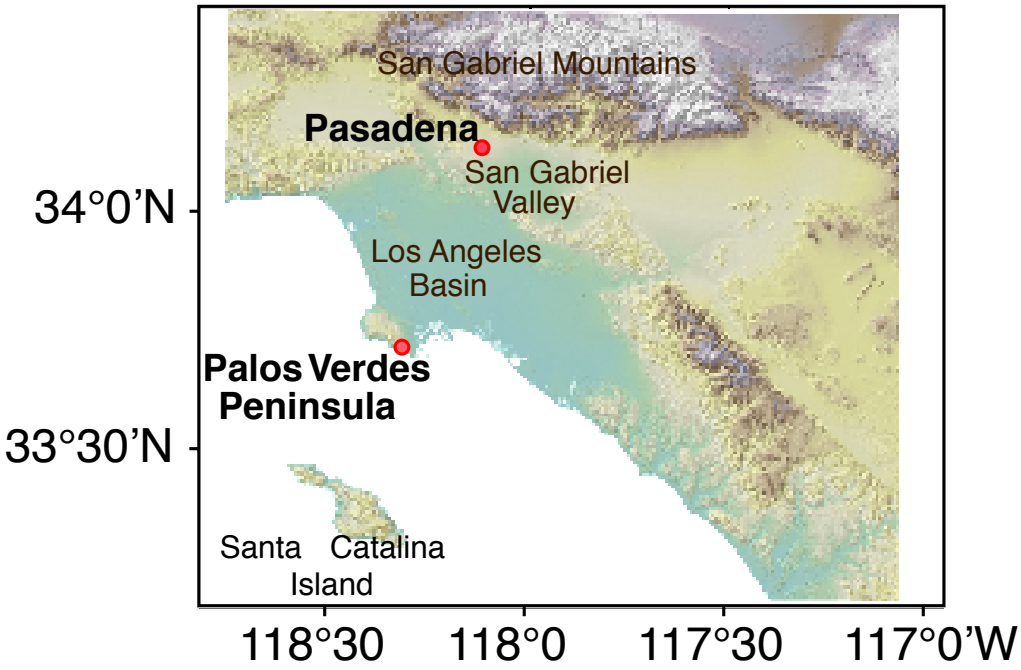

Figure 1. Map of southern California, showing sampling locations in Pasadena and Palos Verdes (red dots).

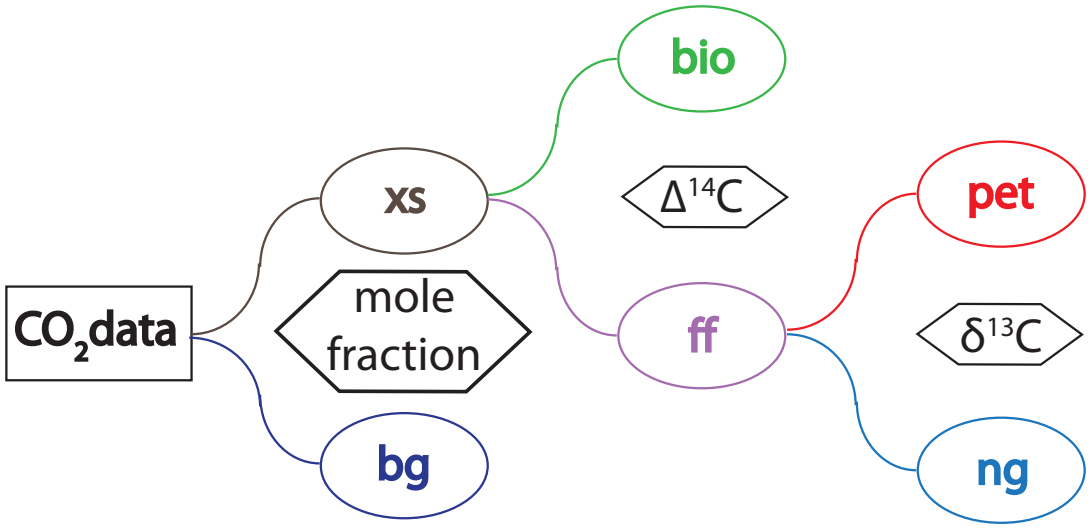

935 Figure 2. Schematic diagram showing the use of different data sets for attribution of the
936 sources of CO_2 emissions. Mole fractions of background (bg) and observations are used
937 to determine C_{xs} (excess over background/bg); $\Delta^{14}C$ values are used to distinguish C_{ff}
938 (fossil fuel, ff) and C_{bio} (biosphere, bio); $\delta^{13}C$ compositions are used to distinguish C_{pet}
939 (petroleum/gasoline, pet) from C_{ng} (natural gas, ng).

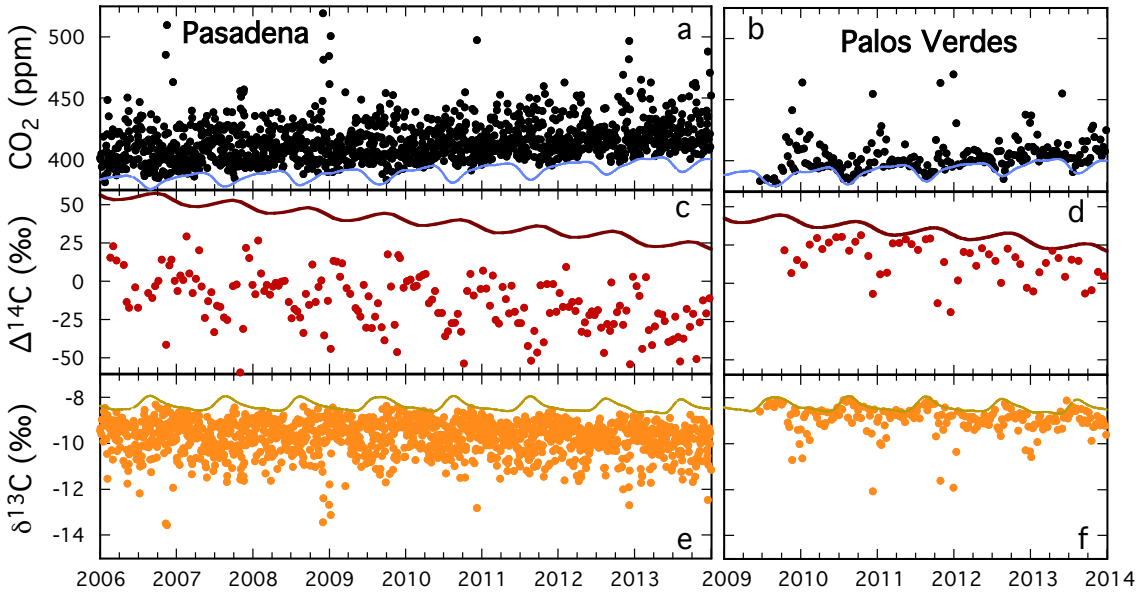

940 Figure 3. Time series of CO_2 mole fractions for $^{14}CO_2$ samples (a, b), $\Delta^{14}C$ data (c, d),
941 and $\delta^{13}C$ (e, f) for Pasadena and Palos Verdes. The solid curves are backgrounds used in
942 the calculations: $\delta^{13}C$ and CO_2 backgrounds are from La Jolla, CA and $\Delta^{14}C$ from Pt.
943 Barrow, AK.

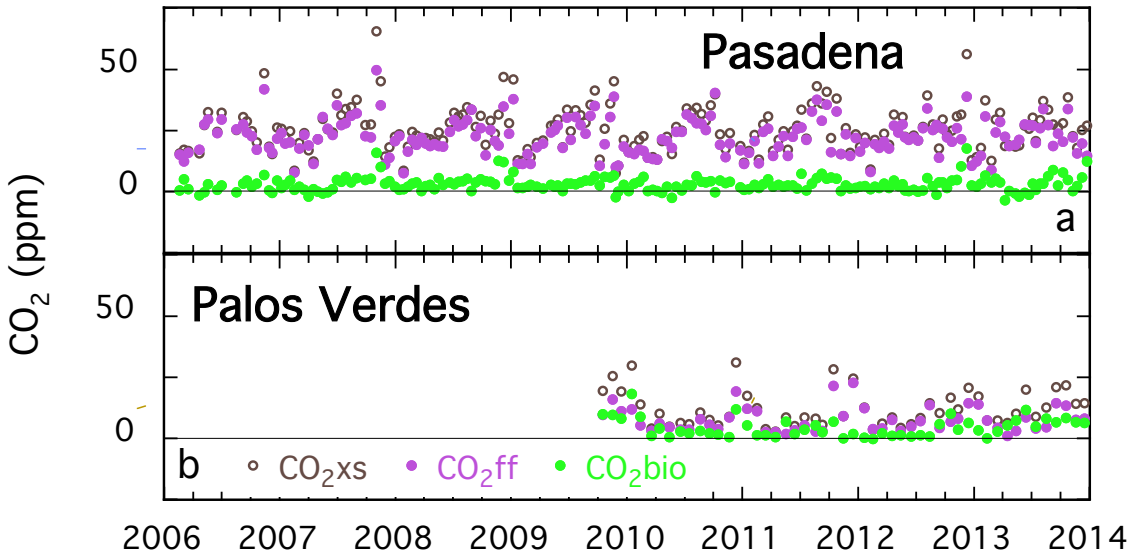

944 Figure 4. Time series of C_{xs}, C_{ff}, and C_{bio} calculated from $\Delta^{14}C$ (see text for description of
945 calculations) for Pasadena (a) and Palos Verdes (b). The errors for C_{ff} are 1 ppm. The
946 negative C_{bio} values indicate photosynthetic uptake. The value of $\Delta^{14}C$ for fuel for this
947 calculation was taken to be -954 ‰, the average from the summer and winter
948 calculations.

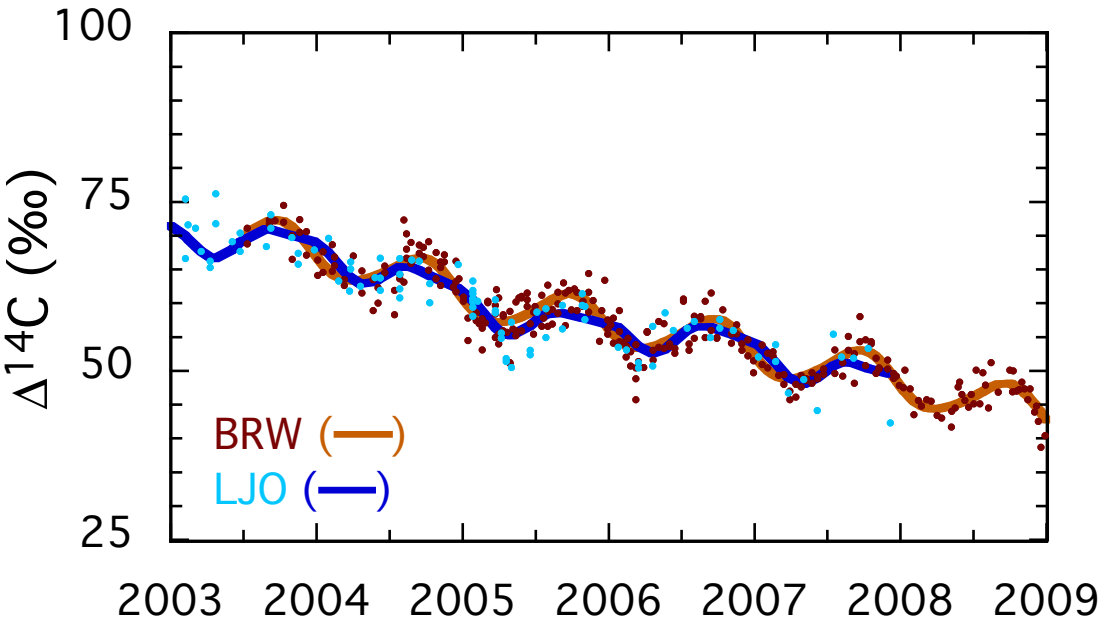

949 Figure 5. Comparison of possible background records for this study, Pt. Barrow, AK,
950 (BRW; Xiaomei Xu, unpublished data) and La Jolla, CA (LJO; Graven et al., 2012). The
951 smoothed brown curve for BRW is the $\Delta^{14}C$ background used for this study and was
952 calculated using the algorithm of Thoning et al. (1989), from the function plus the
953 smoothed residuals of the long-term trend, using 2 harmonic and 3 polynomial terms in
954 the function and 667 days as the long-term cutoff for the low-pass filter.

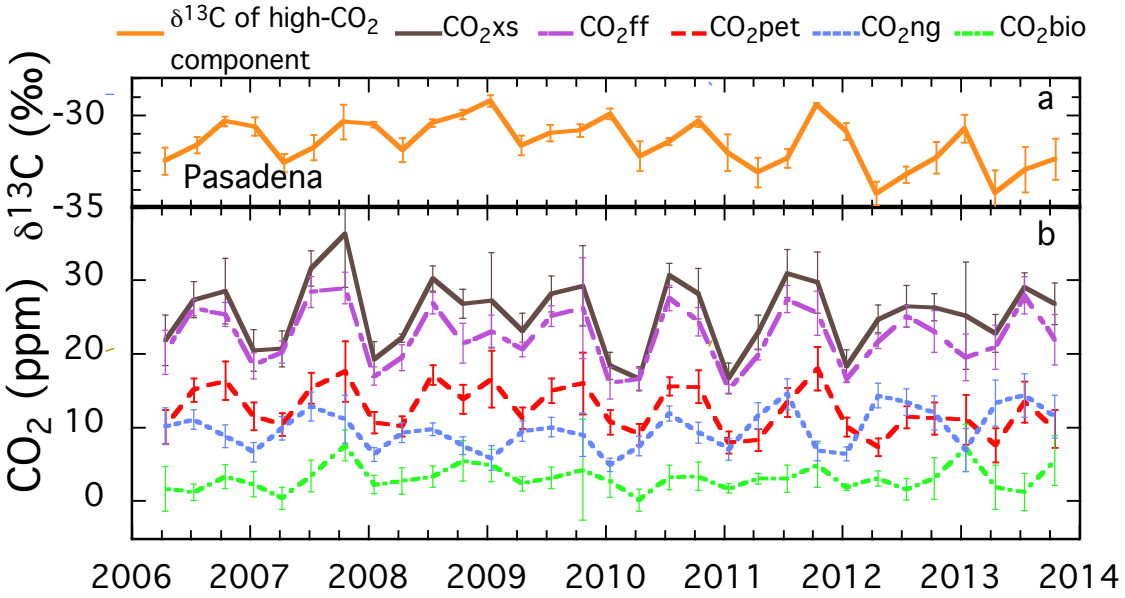

Figure 6. Attribution of CO_2 excess in Pasadena among combustion of natural gas and petroleum and the biosphere. (a) Miller-Tans slopes for seasonal averages of monthly plots. Error bars are standard errors of the regression intercepts. (b) Attribution of C_{xs} among all three sources (natural gas, petroleum, and the biosphere), combining the information from $\Delta^{14}C$ and $\delta^{13}C$, using Miller-Tans slopes to determine the relative proportions of petroleum and natural gas combustion. Error bars are propagated from the errors in the $\delta^{13}C$ intercepts and the $\Delta^{14}C$ measurements.

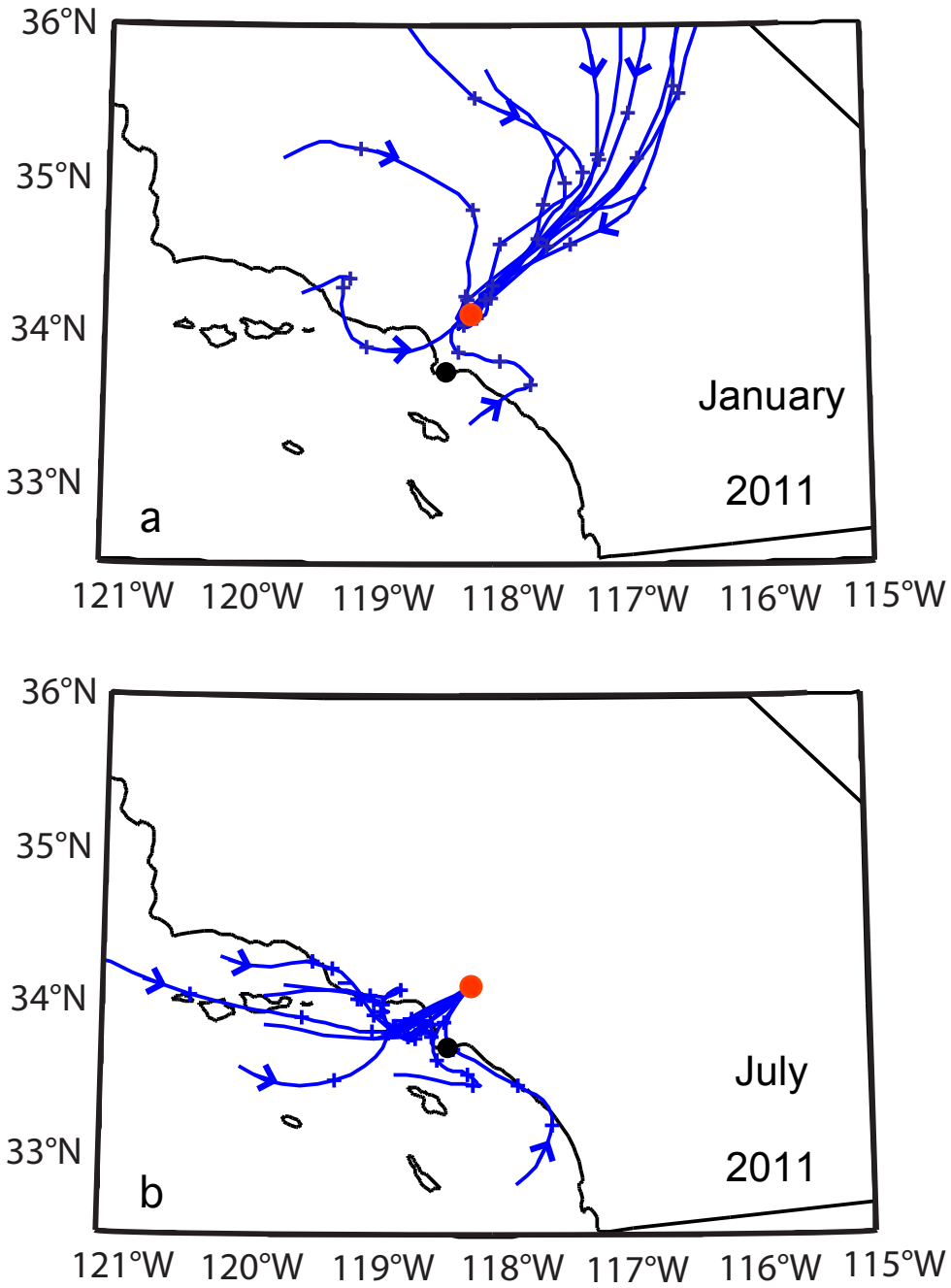

962 Figure 7. Back trajectories (24 hour) for winds arriving at the Pasadena site (red dot) at
963 1400 PST for January (a) and July (b) 2011, calculated by HYSPLIT (Draxler and Rolph,
964 2015; Rolph, 2015) for all sampling days in January and selected sampling days in July,
965 for clarity. Results for all sampling days are shown in Fig. A2. Arrows indicate the
966 direction of air flow. Plus signs indicate 6, 12, and 18 hours from the Pasadena site. The
967 black dot is the location of the Palos Verdes site. The back trajectories for the Palos
968 Verdes site show a similar pattern (Appendix Fig. A2). The back trajectories explain the
969 difference between the annual cycles at the two sites, shown in Fig. 8.

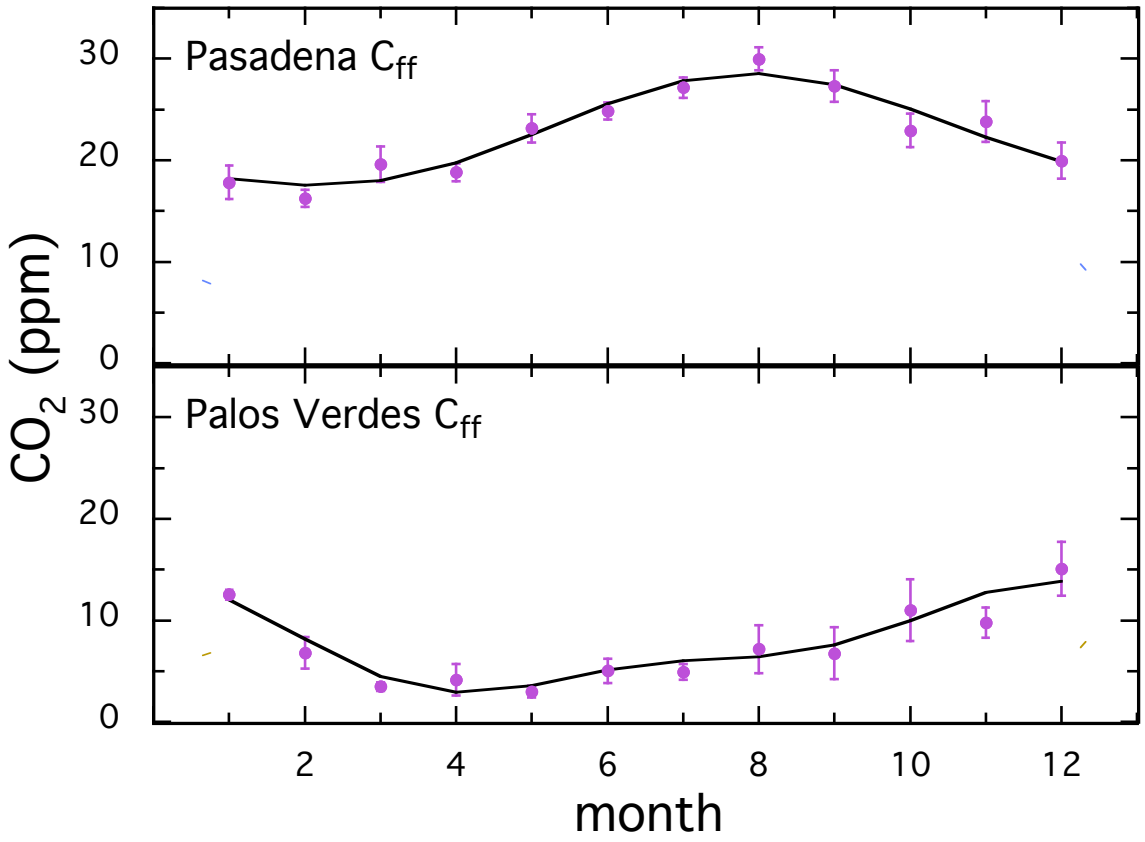

970 Figure 8. The annual patterns for C_{ff} in Pasadena and Palos Verdes calculated as the best
971 fit of two harmonics plus the average of the annual cycles (black curves). These patterns
972 are consistent with seasonal differences in the back trajectories shown in Fig. 7.

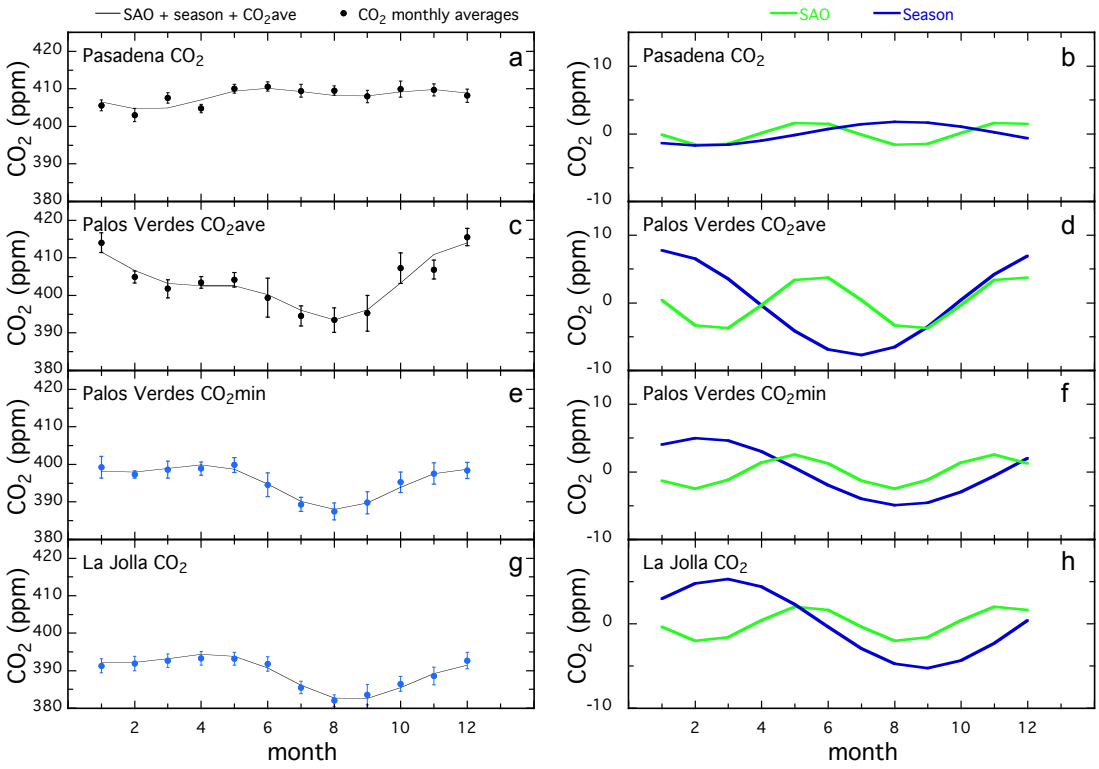

973 Figure 9. Comparison of seasonal and semi-annual oscillation cycles of CO_2 mole
974 fractions for flask samples from Pasadena (2006-2013) with those at the La Jolla (2006-
975 2013) and Palos Verdes (2009-2013) sites. Left column panels show the average annual
976 patterns for the monthly averages together with the sum of the harmonics for seasonal
977 (blue) and semi-annual (green) cycles (Jiang et al., 2008). Right column panels show the
978 amplitudes and phases of the pure harmonic components. Two sets of results are shown
979 for Palos Verdes, for the monthly averages (c, d) and for the monthly averages of weekly
980 minima (e, f). The monthly averages show the effect of transport on the signal, with a
981 large peak during the winter, while the minima (in blue) show that data from this site are
982 very similar to La Jolla (in blue) and should be a good estimation of the background air
983 for the LA basin. Error bars on the monthly averages of the data are 1σ standard errors.

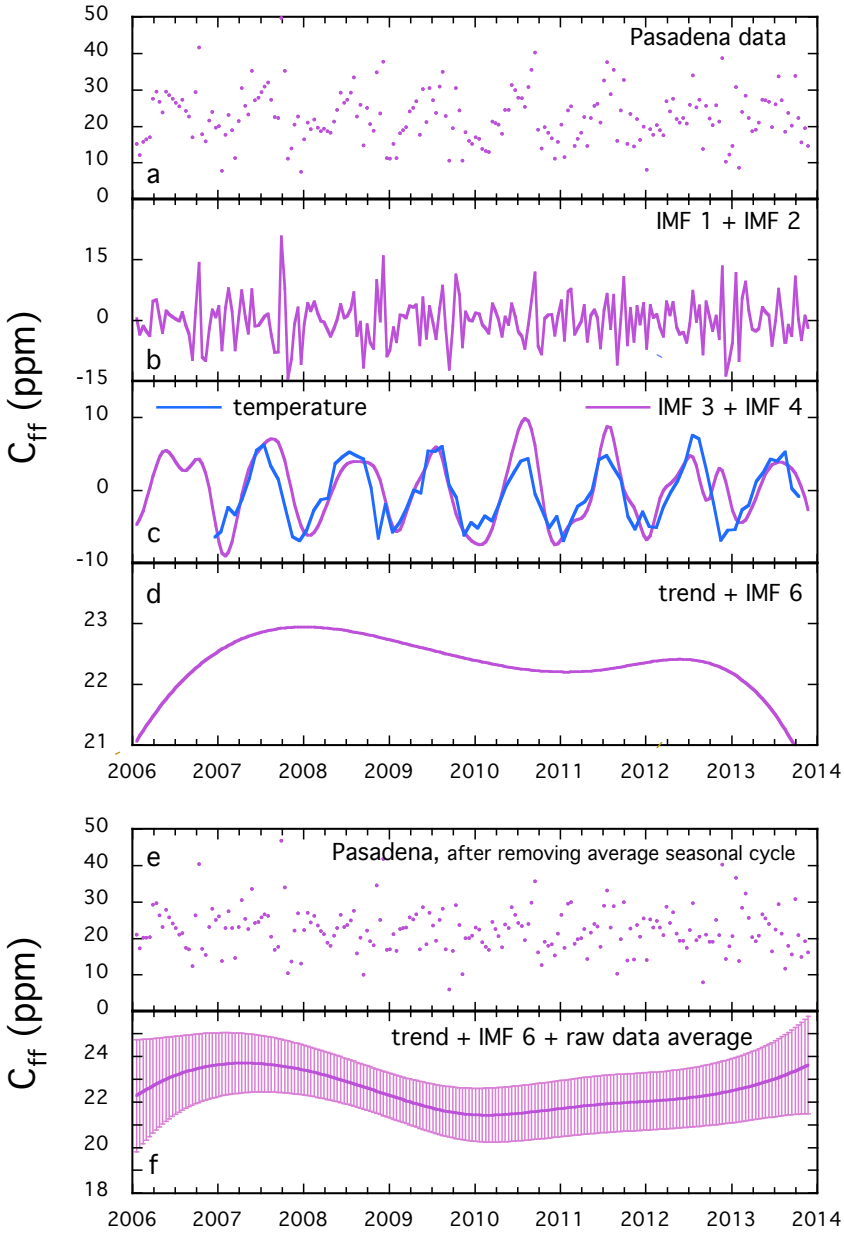

984 Figure 10. Results of ensemble empirical mode decomposition (EEMD) (Huang et al.,
985 1998; Wu and Huang, 2009) of the C_{ff} time series calculated using Eq. (3) and the
986 average, constant $\Delta^{14}C$ of -954 ‰ for fossil fuel. The top set of panels show the raw data
987 (a), noise (b), annual and semi-annual mode (c), and the trend + IMF 6 (d). The pattern
988 of the trend + IMF 6 shown in (d) is within 1σ uncertainty of no variation over this time
989 period. The bottom two panels include the raw data after subtracting the average annual
990 cycle (centered at zero) (e) and the trend + IMF 6 for the modified data set (f). 30-day
991 average temperatures (minus the overall average and scaled to match the magnitude of
992 the C_{ff} IMF; blue curve) are superimposed on the plot of IMF 3 + IMF 4 (c). Shaded
993 regions in (f) indicate 1σ standard deviation of 300 Monte Carlo realizations with 13.7 %
994 noise added, the ratio of the uncertainty in C_{ff} to the standard deviation of the data.

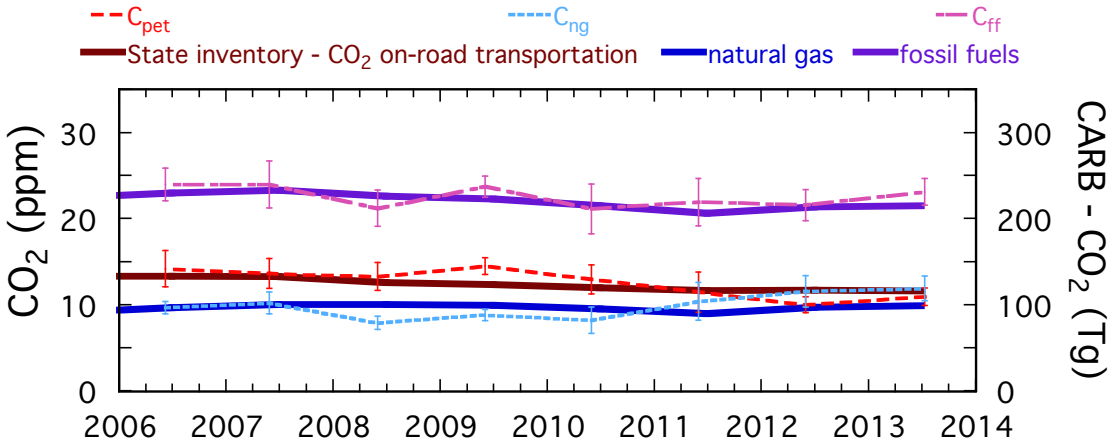

995 Figure 11. Comparison of annual average CO_2 emissions from bottom-up California Air
996 Resources Board (CARB) inventories (thick lines; right axis labels) for fossil fuel-
997 derived emissions with top-down annual averages from the Pasadena data, using the
998 Miller and Tans (2003) approach to attribute CO_2 emissions from petroleum and natural
999 gas combustion from the $\delta^{13}C$ measurements. Annual curves showing the attribution of
1000 C_{xs} averaged from the seasonal values from Fig. 6b are shown as thinner lines. The error
1001 bars on the results from the flask sample data are 1σ standard errors of the means. The
1002 annual trends from the bottom-up CARB inventories are plotted on a scale exactly 100
1003 times that of the trends derived from the CO_2 measurements, showing that the relative
1004 proportions are very similar through 2013.

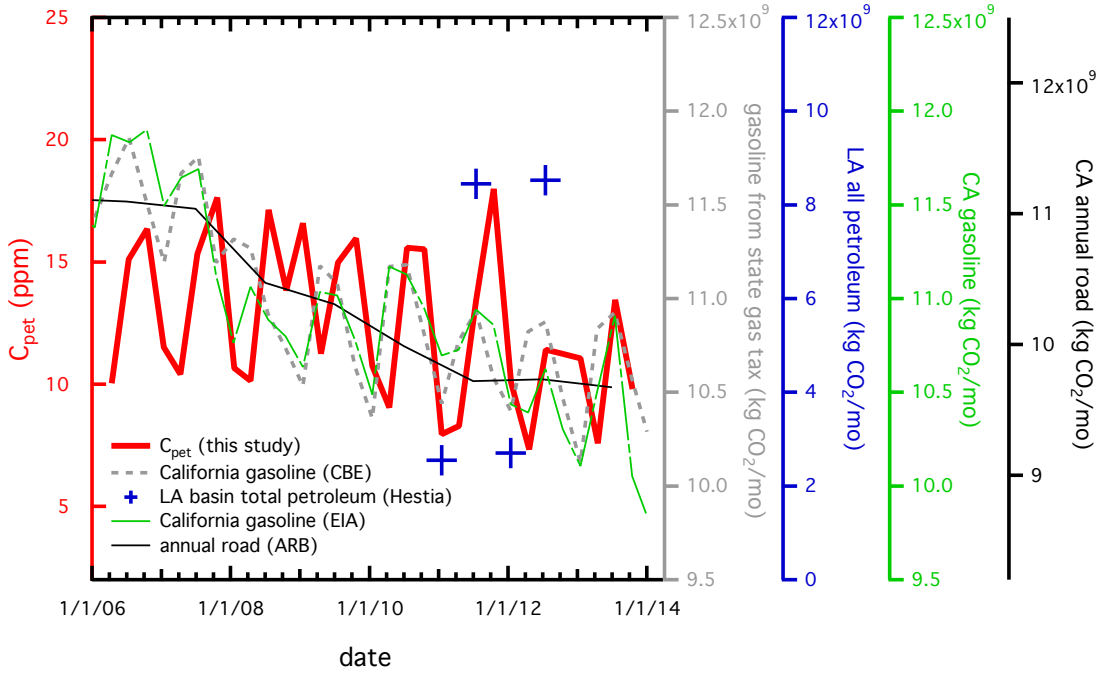

Figure 12. Comparison of the Pasadena C_{pet} atmospheric concentration with all available area-integrated bottom-up fossil fuel CO_2 emissions per month (mo), including gasoline sales based on taxes paid to the California Board of Equalization (CBE, 2014), gasoline provided in California by prime suppliers, the California Air Resources Board's annual road emissions (CARB, 2015), and the Hestia-LA gridded total petroleum. The Hestia-LA data product is specific to the Los Angeles megacity domain; all inventories are statewide estimates. Since the Hestia-LA product is gridded, we show the emissions emanating from different regions for January (northeast quadrant, Fig. 13a) and July (southwest quadrant), based on prevailing winds during those periods (Figs. 7 and 13a). The axis for each inventory has been adjusted to allow easy comparison. The seasonality of the C_{pet} data lags the bottom-up inventories by a few months. This analysis is consistent with the observed decrease in gasoline combustion during 2008-2011.

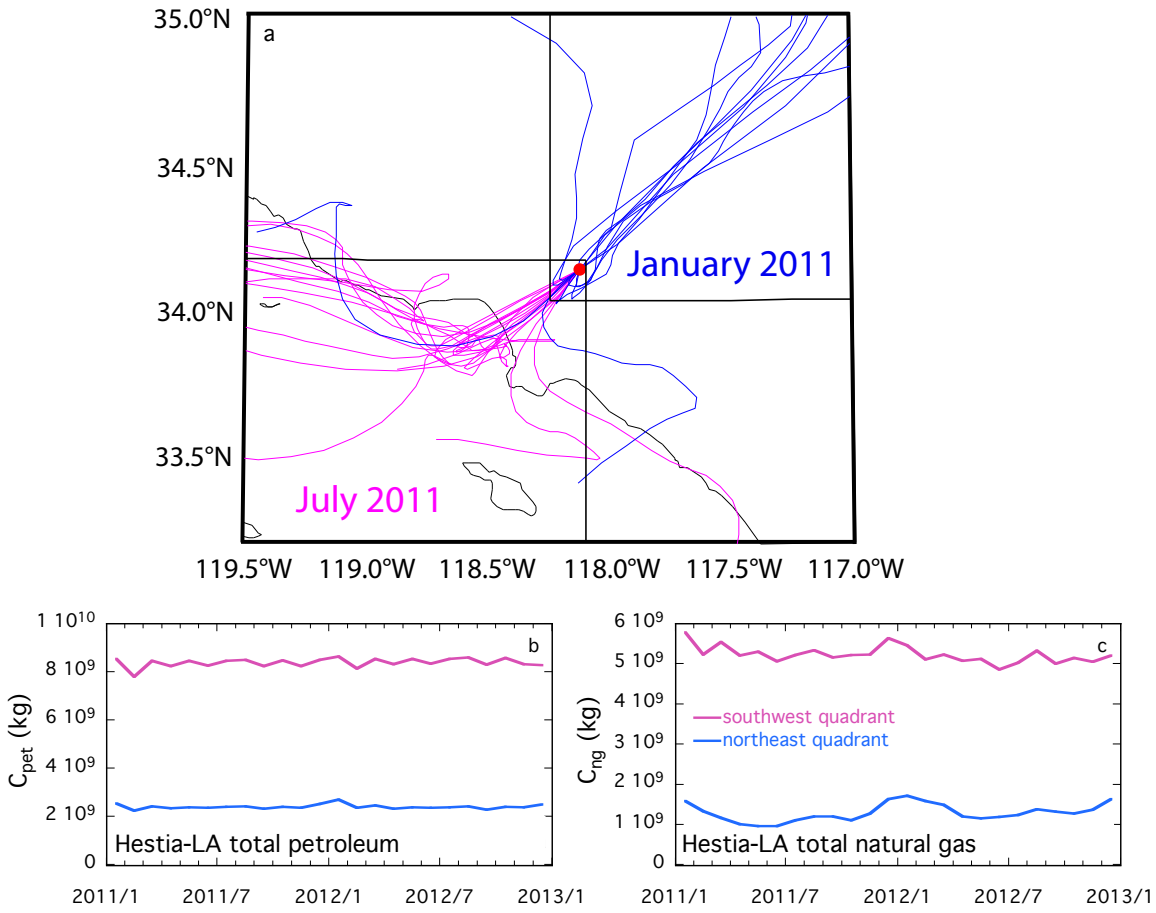

Figure 13. Relevant emissions selection from the Hestia-LA data product. (a) Quadrants selected for investigation of CO_2 emissions from the Hestia-LA data product, together with the 24-hour back trajectories calculated by HYSPLIT for January (northeast quadrant) and July (southwest quadrant) $\Delta^{14}C$ sampling days. The back trajectories end in Pasadena (red dot) at 1400 PST. Monthly averaged time series for Hestia-LA data product C_{ff} are shown from total petroleum combustion (b) and total natural gas combustion (c) for 2011 and 2012. For both the northeast quadrant of the Los Angeles region, the source of winter emissions, and the southwest quadrant, the source of summer emissions, the seasonal pattern is either flat (petroleum) or characterized by peaks during the winter (natural gas). But the summer emissions are always higher than those during winter, consistent with the observed top-down patterns for C_{pet} and C_{ng} in Pasadena.

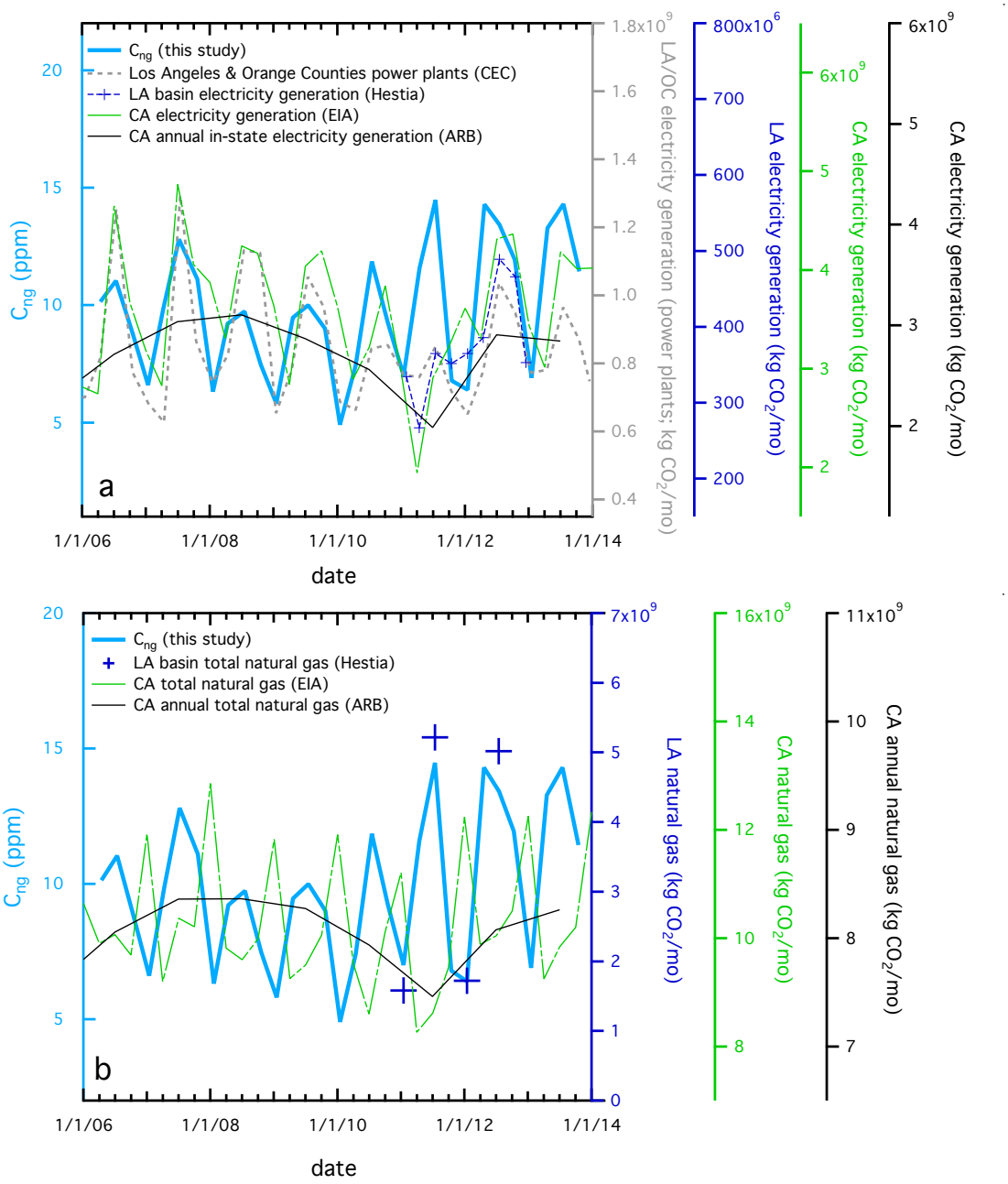

Figure 14. Comparison of Pasadena C_{ng} atmospheric concentration with area-integrated inventories of natural gas combustion, as well as the gridded Hestia-LA data product for southwest and northeast regional sectors for July and January months, respectively, in emissions/month (mo). Panel (a) compares the data from this paper with usage of natural gas by the electrical power sector; panel (b) shows the comparison with total natural gas consumption. Statewide inventories are given by EIA (2014) and CARB (2015) curves. Regional inventories include Hestia results and natural gas from power plants (CEC, 2014) in Los Angeles and Orange counties with monthly data (except Calabasas and Valencia). The vertical axes have been adjusted to allow easy comparison. This analysis is consistent with the increase in natural gas usage during the last few years.

Appendix

1. Monthly Miller Tans plots for 2011

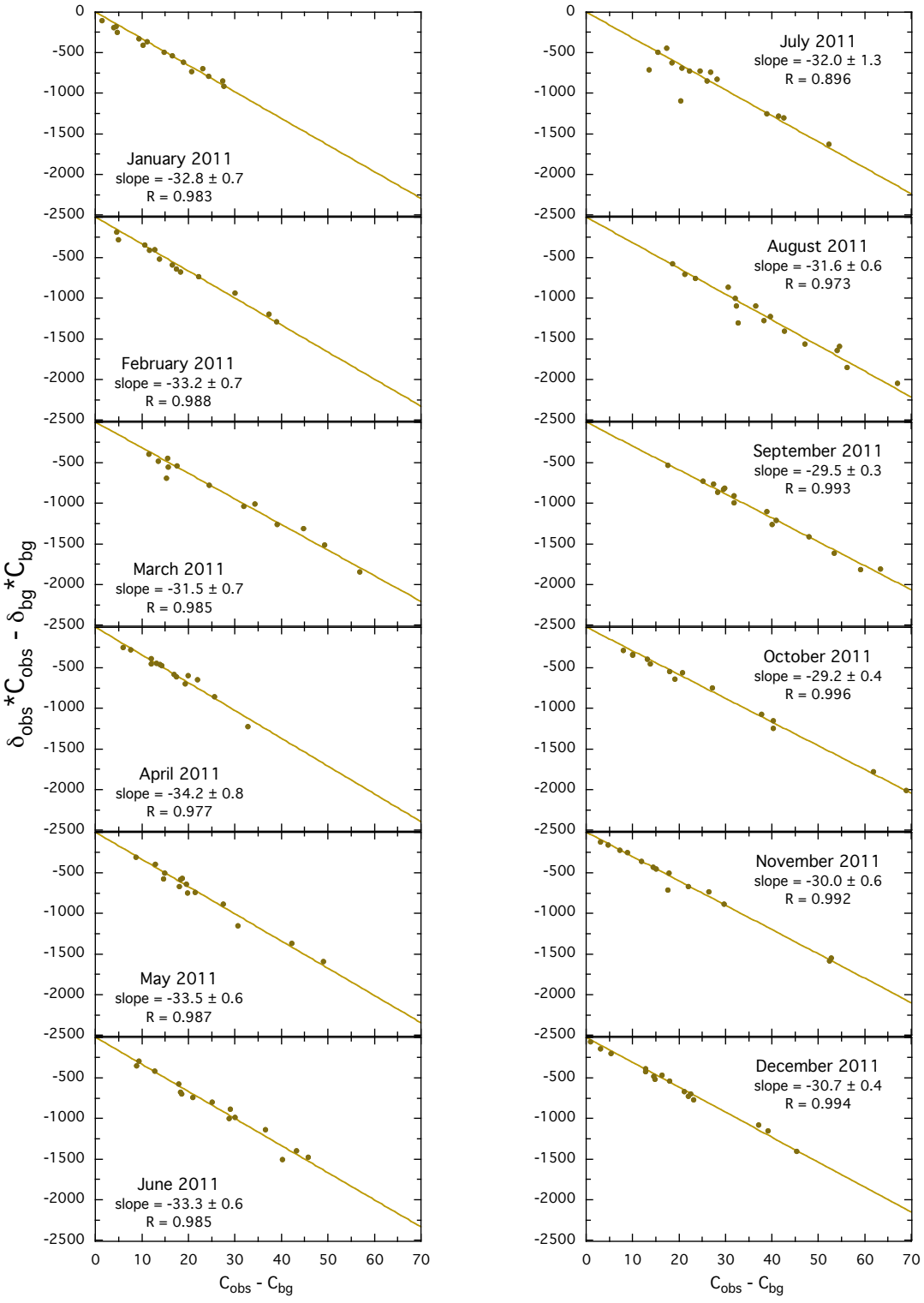

Figure A1. Miller-Tans plots for each month in 2011. Values of the slopes for three-month seasonal averages are plotted in Fig. 6a.

2. Back trajectories for both Pasadena and Palos Verdes sites

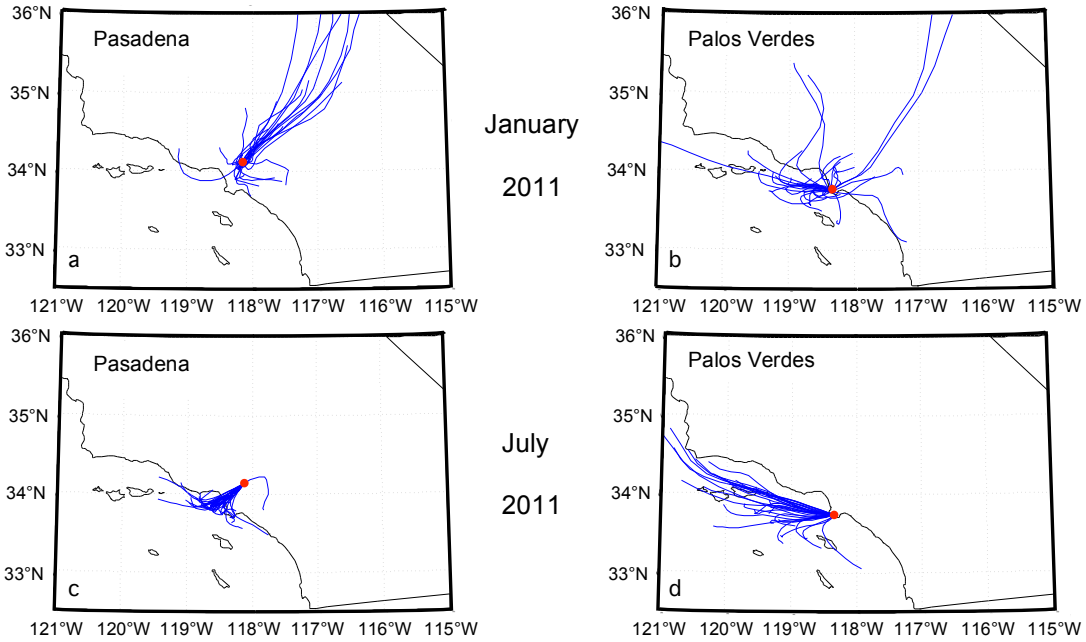

Figure A2. Twelve-hour back trajectories for all days in January and July, 2011, for the Pasadena and Palos Verdes sites. This shows more detail for the effect of transport on the air masses sampled during summer and winter at the Palos Verdes site than Fig. 7.

3. Full ensemble empirical mode decomposition results

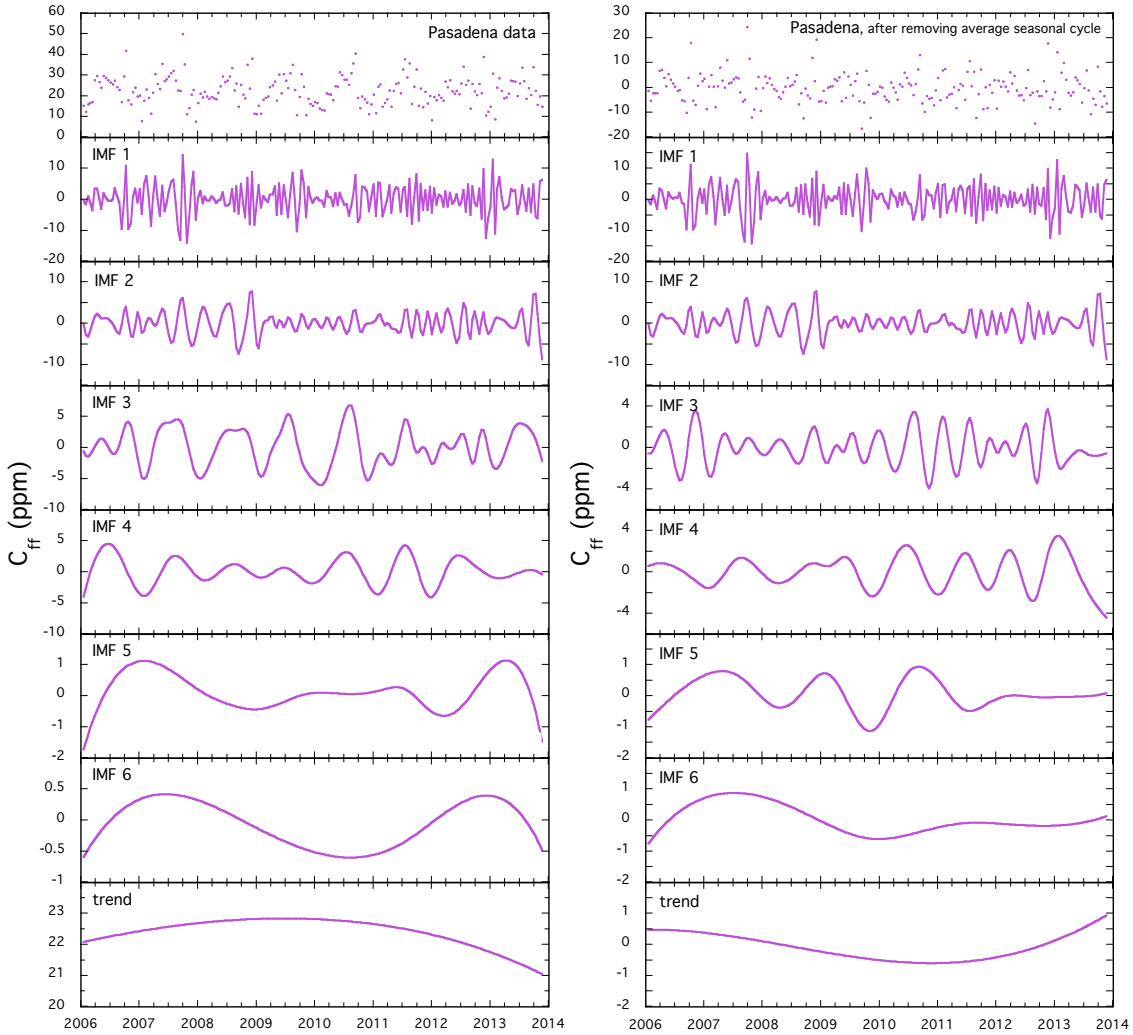

Figure A3. Time series of all of the results from the ensemble empirical mode decomposition (EEMD) analysis of the Pasadena C_{ff}. The left set of panels shows the results for the raw data, whereas the right column shows those for the data after subtraction of the average seasonal cycle. The long-term trend reflecting the economic downturn of the Great Recession is reflected clearly in IMF 6 and the trend of the data after the pronounced seasonality is removed (right-hand column), although there is some evidence of it in IMF 6 of the raw C_{ff} data.